REVIEW

Metal Phosphorus Trichalcogenides

ADVANCED
FUNCTIONA
MATERIALS
www.afm-journal.d
Check for updates

New Frontiers on van der Waals Layered Metal Phosphorous Trichalcogenides

Fengmei Wang, Tofik A. Shifa, Peng Yu, Peng He, Yang Liu, Feng Wang, Zhenxing Wang, Xueying Zhan, Xiaoding Lou,* Fan Xia,* and Jun He*

The exponentially growing works on 2D materials have resulted in both high scientific interest and huge potential applications in nanocatalysis, optoelectronics, and spintronics. Of especial note is that the newly emerged and promising family of metal phosphorus trichalcogenides (MPX$_3$) contains semiconductors, metals, and insulators with intriguing layered structures and architectures. The bandgaps of the members in this family range from 1.3 to 3.5 eV, significantly enriching the application of 2D materials in the broad wavelength spectrum. In this review, emphasizing their remarkable structural, physicochemical, and magnetic properties, as well as the numerous applications in various fields, the innovative progress on layered MPX$_3$ crystals is summarized. Different from other layered materials, these crystals will advance a fascinating frontier in magnetism and spintronic devices with their especially featured atomic layered nanosheets. Thus, their crystal and electronic structures, along with some related researches in magnetism, are discussed in detail. The assortments of growth methods are then summarized. Considering their potential applications, the prominent utilization of these 2D MPX$_3$ nanoscrystals in catalysis, batteries, and optoelectronics is also discussed. Finally, the outlook of these kinds of layered nanomaterials is provided.

1. Introduction

van der Waals layered materials, including graphene,[1] transition metal dichalcogenides (TMDs),[2,3] black phosphorus,[4,5] and boron nitride (BN),[6] dominate the current era of 2D crystals. Given their unique physical and chemical properties, which do not appear in 3D structures, they are widely utilized as electronic and structural materials.[7] Especially, the fabrication of heterostructures and optoelectronic nanodevices using 2D materials has been studied, resulting in extraordinary findings in various fields of study. The electron confinement in the 2D feature endows them with some specific properties, such as charge density wave occurrence,[8] anisotropic magnetic behavior[9] and conductivity,[2,4] anisotropy of photoluminescence,[10] and large surface area. In this regard, TMD materials represent a strikingly indispensable series of 2D crystals. As far as their structure is concerned, strong covalent bonded layers, constituting a cationic plane (M^{4+}) enclosed by two planes of anionic (S^{2-}, Se^{2-}, or Te^{2-}), enlarge into infinite sheets. The arrangement of such S(Se)–M–S(Se) sandwiches provides an empty space, in which two adjacent layers are weakly bonded to each other via the van der Waals (vdW) force.[11,12] Their optical and electronic properties could be controlled by changing the components and the thickness.[13,14] For instance, the bandgap of MoS$_2$ (a typical TMD) can be enlarged from 1.29 to 1.9 eV via reducing the thickness from multilayers to a monolayer.[13,15] Although their bandgaps can be tuned, TMDs are generally characterized by small bandgaps (smaller than 2.02 eV),[16] which limits their application in devices requiring values beyond this range. Thus, 2D materials exhibiting bandgaps ranging from 2.02 to 4.0 eV are extensively sought to meet the application requirements in the broad wavelength spectrum.

Nowadays, a burgeoning research direction goes toward the newly emerged van der Waals layered materials known as metal phosphorus trichalcogenides (MPX$_3$). The metal cations (M^{II} or M^{I}M^{III}) stabilize [P$_2$S$_6$]$^{4-}$ or [P$_2$Se$_6$]$^{4-}$ framework layers weakly bonding each other via vdW interactions. This family contains a variety of transition metal phases, ranging from vanadium to zinc (M = V, Mn, Fe, Co, Ni, Zn, etc.) in the first row, partial alkaline metal in group-II, and some other metal

Dr. F. M. Wang, Dr. T. A. Shifa, P. He, Y. Liu, Dr. F. Wang, X. Zhan, Prof. Z. Wang, Prof. J. He
CAS Center for Excellence in Nanoscience
CAS Key Laboratory of Nanosystem and Hierarchical Fabrication
National Center for Nanoscience and Technology
Beijing 100190, China
E-mail: hej@nanoctr.cn

The ORCID identification number(s) for the author(s) of this article can be found under https://doi.org/10.1002/adfm.201802151.

Dr. T. A. Shifa, P. He, Y. Liu, Prof. J. He
University of Chinese Academy of Sciences
Beijing 100049, P. R. China

P. Yu, Prof. X. Lou, Prof. F. Xia
Engineering Research Center of Nano-Geomaterials of Ministry of Education
Faculty of Materials Science and Chemistry
China University of Geosciences
388 Lumo Road, Wuhan 430074, P. R. China
E-mail: louxiaoding@cug.edu.cn, xiafan@cug.edu.cn

ions. Friedel[17] and Ferrand[18,19] discovered them in the late 1800s. Based on the interesting structure of these materials, significant research works were reported in the early 2000s. As expected, 2D MPX_3 phases share most of the abovementioned specific properties of 2D TMDs. According to the theoretical and experimental results, MPX_3 compounds are the most sought functional materials for their intermediate bandgaps ranging from 1.3 to 3.5 eV,[20,21] indicating their enhanced light absorption efficiency as compared to the TMD materials. In addition, their unusual intercalation-substitution or intercalation-reduction behavior as well as the incipient ionic conductivity promote their usage in Li-ion batteries,[22,23] gas storage,[24] and photo-electrochemical reactions.[25] Unlike TMDs, several MPX_3 materials show intrinsic anti-ferromagnetism below the Neel temperatures of 78 K for $MnPS_3$, 116 K for $FePS_3$, and 155 K for $NiPS_3$.[26,27] Recently, Li et al.[28] predicted that transformation from the anti-ferromagnetism to ferromagnetism for exfoliated $MnPSe_3$ nanosheet will be reduced by carrier doping. And the Monte Carlo simulation reveals the Curie temperature of the doped $MnPSe_3$ nanosheets can reach 206 K, rendering it with potential for utilizations in spintronic devices at high temperature. Therefore, the members in the MPX_3 family have the abovementioned properties along with structural flexibility stemming from their van der Waals nature; thus, it is reasonable to assume that they will contribute to the next major frontier in 2D vdW layered materials.

Herein, we emphasize on reviewing the impressive recent progress and thoughts on physical and chemical characteristics, specific properties, growth methods, and potential applications of 2D MPX_3 crystals. The structure of MPX_3 is comprehensively described and compared with the common TMD's structure. According to the variety of cations (M) and their corresponding valence states, they are categorized into M^{II}, $M^{I}M^{III}$ and other component-based MPX_3 materials. The bandgaps, crystal structures, and stacking of layers are summarized for tangible deduction on the materials functionality and specific properties. Furthermore, the material functionality and specific properties of MPX_3 are also discussed. Up to now, the synthesis of 2D ultrathin MPX_3 crystals has been a big challenge. Therefore, we are inclined to summarize the growth of atomic layered MPX_3 crystals. Considering the feature-based application of this type of layered crystals, we also introduce some applications. The final section of this review contains future perspectives of these types of 2D layered materials.

1.1. Composition and Crystal Structures

All the members in the family of MPX_3 materials share a defining common structural feature such that $(P_2S_6)^{4-}$ or $(P_2Se_6)^{4-}$ anion sublattice appears within each layered crystal. The honeycomb arrangement of the transition metal ions is distributed around the $(P_2X_6)^{4-}$ bipyramids. Thus, these compounds are usually described as $M_2P_2S_6$. A structural comparison between typical layered MoS_2 and MPX_3 is shown in **Figure 1**. In general, the vdW gap (shortest distance between the S layers) distance of the MPX_3 crystals with the first row transition metal elements is around 3.22–3.24 Å, much wider than that of MS_2 ones. Various atomic radii cations can be

Fengmei Wang received her B.S. degree in applied chemistry from Hunan University, China, in 2012. Then she received her Ph.D. degree in physical chemistry from the University of Chinese Academy of Sciences at the National Center for Nanoscience and Technology (NCNST), China, in 2017. From then on, she worked in NCNST as an assistant professor. Her major research interests include synthesis and development of novel 2D materials, such as transition metal chalcogenides, meal phosphorous trichalcogenides, etc., for electrocatalysis or photocatalysis.

Tofik A. Shifa received his B.S. degree in applied chemistry from Arbaminch University, Ethiopia in 2007. He then obtained his M.S. degree in analytical chemistry from Haramaya University, Ethiopia in 2011. He has recently got a Ph.D. degree in physical chemistry from the University of Chinese Academy of Sciences at the National Center for Nanoscience and Technology (NCNST), Beijing, China. His research focuses on the controllable synthesis of 2D layered materials for water splitting.

Jun He received his Ph.D. in semiconductor physics from the Institute of Semiconductors, Chinese Academy of Sciences (CAS), in 2003. Then he worked successively at the Applied Physics Department of Technische Universiteit Eindhoven, Netherlands, The Material Department of University of California, Santa Babara, and California NanoSystem Insitute (CNSI), University of California, Los Angeles, USA. He joined the "100-Talents" Program of CAS in November 2010 and became a full professor of NCNST since then. Jun's main research interests are the synthesis, characterization, and devices of low dimensional semiconductor materials.
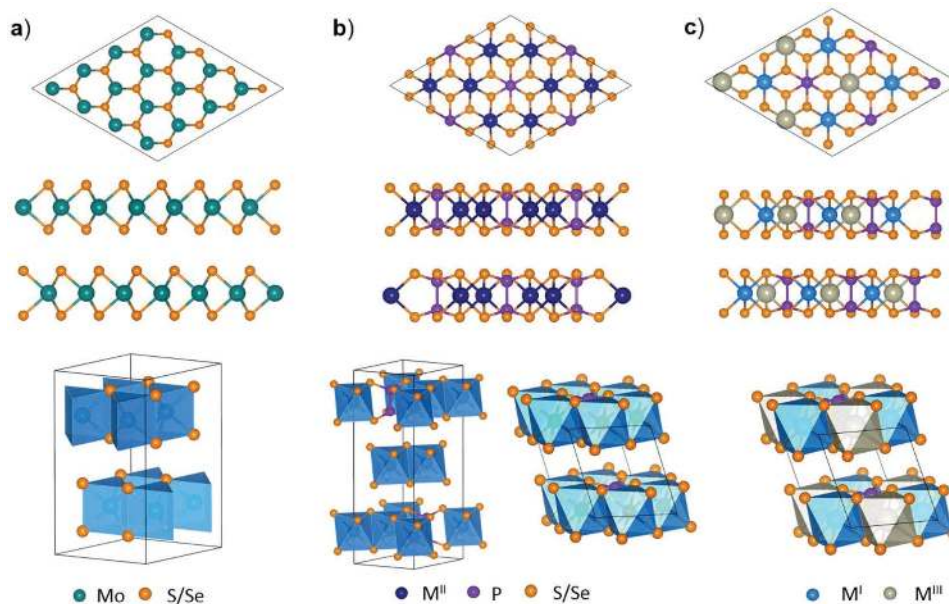
Figure 1. Comparison of crystal structures, including the top view (top), side view with two layers (middle), and crystal phase, of a) MoS_2 with hexagonal crystal, b) $M^{II}PX_3$ with hexagonal (left) and monoclinic(right) crystals, and c) $M^{I}M^{III}PX_3$ with monoclinic crystal. Here, the 2H phase of MoS_2 is taken as an example.

located in the MPX3 along with the change of the slab size. As to the $P_2S_6^{4-}$ structural modification, the flat pyramid constituting S^{2-} ions remains invariable but the P−P distance is somewhat elongated to accommodate the different metal cations. There is a shift, regardless of the type of M cations, from 2.148 Å ($NiPS_3$) to 2.222 Å ($CdPS_3$) for P−P distance in MPS_3 crystals.[29] However, the layer thickness is positively related to the value of the P−P distances for MPX_3 crystals.[30] The component of MPX_3 can be tuned by changing the M and X atoms. On the anion side, $P_2S_6^{4-}$ and $P_2Se_6^{4-}$ anions can be alloyed in the $M_2P_2X_6$ structure. Mixed chalcogen, in which the various atoms (i.e., S or Se) are alloyed with each other, is adopted. Some alloys, such as $Ni_2P_2S_{6-x}Se_x$,[31] $CuInP_2S_{6-x}Se_x$,[27,32] $MnPS_xSe_{3-x}$,[33] and $Sn_2P_2S_{6-x}Se_x$,[34] have been studied. On the cation side, MPX_3 can accommodate group II elements (e.g., Mg), group IV elements (e.g., Sn), transition metals (i.e., Sc, Mn, Fe, Co, Pd, Ag, and Cd, etc.), or a combination thereof. Until now, the most studied materials are Mn, Fe, and Ni based MPX_3 compounds due to their magnetic ordering and applications in electrochemistry and catalysis.[20,35,36] From the component point of view, it constitutes a potentially broad material class. **Figure 2** shows metal elements in the periodic table that are known to crystallize into MPX_3 type materials. In the following sections, these MPX_3 crystals will be classified according to the different cations and described in detail.

1.1.1. M^{II} Based MPX_3 Crystals

Divalent metal atom-based $M^{II}PX_3$ crystals are common and intensively studied presently. Notably, this aspect is one of particularities to distinguish $M^{II}PX_3$ from $M^{IV}X_2$ (e.g., MoS_2) compounds. The MPS_3 phases are taken as layered MS_2 crystals with one third of the M sites substituted by P−P pairs (P_2), i.e.,

$M_{2/3}(P_2)_{1/3}S_2$. The sulfur atoms comprise the surfaces within individual lamella. From **Figure 3**a, an octahedrally coordinated configuration can be visualized in which the 2/3 is filled by M^{II} cations and the remaining 1/3 is occupied by P−P dimers. The P−P dimers are covalently bonded to six sulfur atoms to form an ethane-like $(P_2S_6)^{4-}$ unit, where each P atom is tetrahedrally coordinated with three S atoms. Meanwhile, a sulfur atom is coordinated with two M^{II} sites and is covalently bonded to one P atom.

Generally, the overall structure of the individual lamella is similar across the MPX_3 family members, but their stacking arrangements in bulk vary depending on the cations and anions constituting the crystals. Their symmetry and lamellar stacking are summarized in **Table 1**. There is an obvious distinction between the sulfides and selenides encountered in their symmetry and crystal structures. The widest symmetry of $M^{II}PS_3$ is C2/m with monoclinic crystal structure, but $HgPS_3$ crystallizes into a space group of $P1$[37] along with distorted tetrahedrally coordinated Hg ions.[30] In the C2/m space group, the structure is constructed from sulfur cubic close-packed arrays with the octahedral sites in each layer completely filled by M^{II} and P−P pairs at a 2/1 ratio. One observes that the value of monoclinic angle β, varying from 106.97° for $MgPS_3$ to 107.35° for $MnPS_3$, is different based on M cations (Figure 3b). For an undistorted monoclinic cell, the value of β is calculated to be 107.16°, suggesting that $CoPS_3$ and $FePS_3$ possess a perfect cell.[38] All $M^{II}PX_3$ materials with the C2/m space show a layers stacking sequence of "AAA" (Table 1).

For $M^{II}PSe_3$ (e.g., $CdPSe_3$, $MgPSe_3$, $FePSe_3$, $ZnPSe_3$), owing to the enlarged P−Se bond distance and Se−P−Se bond angles, their space group has been reported as $R3(-)h$.[39–41] The distortions exhibited in the PSe_3 groups on the bottom halves of one layer result in the lack of an inversion center for these $MPSe_3$ crystals. Otherwise, $NiPSe_3$ has the same symmetry as that of

Figure 2. The metal atoms and their valence states constituted in MPX_3 crystals in the periodic table of elements. Filled blocks represent elements for which the layered MPX_3 structure has been reported to form.

$NiPS_3$ (C2/m). Based on the above descriptions, most selenides crystallize into monoclinic or trigonal crystallographic structures. The $M^{II}PSe_3$ crystals with $R\bar{3}h$ symmetry demonstrate the lamellar stacking sequence of "ABC" (Table 1). $Hg_2P_2Se_6$ adopts a unique structure with tilting of P—P dimers, distorting the octahedral cages between the P_2Se_6 units, and its stacking sequence is "ABAB."

For layered MPX_3 crystals, their interlayer distances (d, i.e., distance between two layers) vary from 6.3 to 6.7 Å (Figure 3c). The ordering of d, namely, $d_{MnPS3} > d_{FePS3} > d_{NiPS3}$, is same as that of the M radius (r) ($r_{Mn} > r_{Fe} > r_{Ni}$). Additionally, selenides possess a larger interlayer distance than that of the corresponding sulfides, like $d_{MnPSe3} > d_{MnPS3}$.

1.1.2. Polymetallic MPX_3 Compounds

The "M" atoms in MPX_3 crystals could be substituted by other metal atoms, including homocharge and heterocharge substitution. If the size of M_1^{II} and M_2^{II} cations is almost the same, the homocharge substitution will be realized easily. For example, a series of $Zn_{1-x}Fe_xPS_3$, $Zn_{1-x}Ni_xPS_3$ ($0 \leq x \leq 1$),[29] and $Cd_xFe_{1-x}P_2S_6$ ($0 \leq x \leq 1$)[42] has been obtained. Significantly, the MPX_3 structural type also shows that one M^{II} could be replaced by a couple of heterocharge metal atoms, namely, $1/2$ M_I and $1/2$ M_{III}. M_I includes Ag^+, Cu^+, and M_{III} contains In^{3+}, V^{3+}, Sc^{3+}, and Cr^{3+}, etc. The structure of the mixed-cation $M^I M^{III}[P_2S_6]^{4-}$ compounds is easily tuned. In the 1980s, the synthesized $AgInP_2S_6$[43] and $AgScP_2S_6$[42] crystals were identified as trigonal ($P\bar{1}3c$) and centrosymmetric structures at room temperature. Of special note is that the Cu^+ cations based $CuM^{III}P_2S_6$ compounds are unique. For instance, there are three possible Cu^+

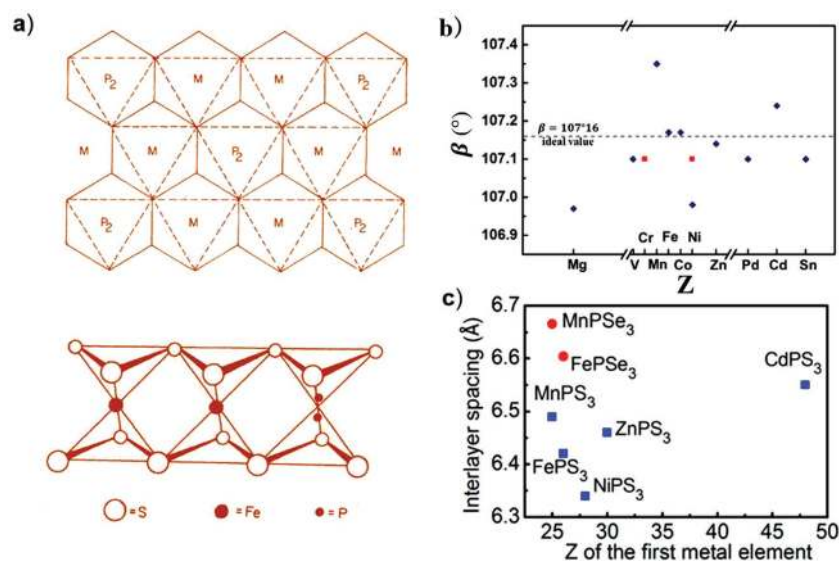**Figure 3.** a) Structure of $FePS_3$, showing the close structural coordination around the Fe^{2+}. Reproduced with permission.[51] Copyright 2018, American Physical Society. b) MPS_3 monoclinic cell β value variation respective to the M^{2+} cation. MPS_3, dark blue "♦"; $MPSe_3$, red "■". c) Interlayer spacings of MPS_3 and $MPSe_3$. Reproduced with permission.[20] Copyright 2016, American Chemical Society.

Table 1. Structural information for the 2D layered $M^{II}PX_3$ crystals.

Components		S based				Components		Se based			
		Crystal structures	Space group	Stacking[a]	Ref.			Crystal structures	Space group	Stacking[a]	Ref.
M^{II}	$ZnPS_3$	Monoclinic	C2/m	AAA	[117]		$ZnPSe_3$	Rhombohedral	$R\overline{3}$	ABC	[89]
	$CdPS_3$	Monoclinic	C2/m	AAA	[18]		$CdPSe_3$	Rhombohedral	$R\overline{3}$	ABC	[41]
	$MnPS_3$	Monoclinic	C2/m	AAA	[18]		$MnPSe_3$	Rhombohedral	$R\overline{3}$	ABC	[39]
	$FePS_3$	Monoclinic	C2/m	AAA	[18]		$FePSe_3$	Rhombohedral	$R\overline{3}$	ABC	[39]
	$NiPS_3$	Monoclinic	C2/m	AAA	[41]		$NiPSe_3$	Monoclinic	C2/m	AAA	[41]
	VPS_3	Monoclinic	C2/m	AAA	[89]		$VPSe_3$	–	–	–	–
	$CrPS_3$	–	–	–	–		$CrPSe_3$	Monoclinic	C2/m	AAA	[41]
	$CoPS_3$	Monoclinic	C2/m	AAA	[89]		$CoPSe_3$	–	–	–	–
	$MgPS_3$	Monoclinic	C2/m	AAA	[89]		$MgPSe_3$	Rhombohedral	$R\overline{3}$	ABC	[89]
	$PdPS_3$	Monoclinic	C2/m	AAA	[89]		$PdPSe_3$	–	–	–	–
	$SnPS_3$	Monoclinic	C2/m	AAA	[118]		$SnPSe_3$	–	–	–	–
	$HgPS_3$	Triclinic	$P\overline{1}$	AAA	[37]		$HgPSe_3$	Monoclinic	C2/c	ABAB	[37]

[a] The c stacking direction; – denotes data not mentioned in the publications.

sites in $CuInP_2S_6$ and the temperature could affect the occupancy.[44] The Cu atom hopping motions have indirectly been proved with single-crystal X-ray diffraction. When the temperature is above 315 K, the Cu^I occupancy splits evenly into the upper and lower sites. Otherwise, the upper site is preferentially filled at $T < 315$ K. Compared to the midplane of the lamella, the Cu^I cations were shifted upward by 1.58 Å, while the In^{III} shifted in the opposite direction by 0.2 Å. Two polar sublattices, which are formed by partial compensation of the two different cations, produce ferrielectric materials due to the huge spontaneous polarization in the stacking direction. However, in $CuCrP_2S_6$ and $CuVP_2S_6$ crystals, the shifts and transitions are different.[45,46] Of the $M^I M^{III} P_2 S_6$ crystals, most of them exhibit an ABAB stacking sequence with various space groups. Notably, $AgVP_2S_6$ and $AgCrP_2S_6$ compounds have buckled crystal structures, likely resulting from the much larger Ag^+ (1.15 Å) ions than the Cr^{3+}(0.62 Å) and V^{3+} (0.64 Å).[47] Thus, Ag atoms do not vary their locations within the sulfur-defined octahedral but they are limited to the center of the layers. Similarly, $M^I M^{III} P_2 Se_6$ shows the structures that are depicted in Figure 1. The compounds of $CuAlP_2Se_6$, $AgAlP_2Se_6$, and $AgCrP_2Se_6$ are reported to exhibit random cation ordering, which does not exist in the other alloyed compounds. Their crystal structure and stacking sequences are shown in **Table 2**. Exceptionally, the existence of three temperature phases (**Figure 4**) occur in $CuBiP_2Se_6$.[48] Their stacking sequences are ABAB (298 K, $P3(\text{-})c$), ABCDEF (173 K, $R3(\text{-})h$), and ABCDEFGHIJKL (97 K, $R3(\text{-})h$)), respectively, suggesting the extended stacking of six to twelve layers before the observed translational symmetry at low temperature.

1.2. Unique Properties of MPX3 Compounds

Owing to the special crystal structure of MPX_3 compounds, many important features, including electrical, magnetic, and optical properties, are demonstrated.[30] On the one hand, the number of electrons in the outmost shell or d orbital of the metal elements constituted in MPX_3 contributes to their unique properties. On the other hand, the $[P_2X_6]^{4-}$ provides a weak ligand field, resulting in a high spin state of the metal atoms.[49,50] Accordingly, a plethora of results about the magnetism of these materials are published from the perspective of experiments and calculations. The electronic configuration varies corresponding to the different cations. These features will be discussed in the following section.

1.2.1. Electronic Structure

The fascinating electronic band model of MPX_3 layered compounds aroused extensive attention in 1980s.[51] The electronic energy-band scheme of the MPX_3 family, e.g., $MnPS_3$, $FePS_3$, and $NiPS_3$, has been studied through the vacuum ultraviolet reflectivity spectra and X-ray absorption spectra. In terms of the molecular orbital and crystal-field theories, Khumalo and Hughes[51] found that high-spin divalent M ions are octahedrally coordinated, and the octahedral ligand of $[P_2S_6]$ field splits the d^5 (Mn^{2+}) orbitals into t_{2g}^3 and e_g^2, d^6 (Fe^{2+}) orbitals into t_{2g}^4 and e_g^2, and d^8 (Ni^{2+}) orbitals into t_{2g}^6 and e_g^2. The energy level scheme shown in **Figure 5**a[50] demonstrates the energy level of $[P_2S_6]^{4-}$ clusters and the localized $3d$ levels of M^{II} ions. Irrespective of the metal $3d$ levels, the valence band and conduction band edges consist of the bonding and the antibonding levels derived from the P−P bonds. In the ionic band-model scheme with divalent metal cations, the P−P pair possesses a valence of +8, suggesting that one electron in P atom contributed to the formation of chemical bond between two P atoms.[51] This electronic structure calculated from the ionic extreme of the Wilson–Yoffe band model was adopted to explain the unusual optical absorption spectra, which reveals that the MPS_3 compounds exhibit semiconducting

Table 2. Structural information for the 2D layered $M^IM^{III}PX_3$ crystals.

		S based				Se based			
	Components	Crystal structures	Space group	Stacking[a]	Ref.	Components	Crystal structures	Space group	Stacking[a]	Ref.
M^IM^{III}	$CuInP_2S_6$	Monoclinic	C2/c	ABAB	[45]	$CuInP_2Se_6$	Trigonal	$P\bar{3}1c$	ABAB	[119]
	$AgInP_2S_6$	Trigonal	P31c	ABAB	[43]	$AgInP_2Se_6$	Trigonal	$P\bar{3}1c$	ABAB	[119]
	$CuCrP_2S_6$	Monoclinic	C2/c	ABAB	[120]	$CuCrP_2Se_6$	Monoclinic	C2/m	AAA	[119]
	$CuVP_2S_6$	Monoclinic	C2	AAA	[46]	$CuVP_2Se_6$	–	–	–	–
	$AgScP_2S_6$	Trigonal	$P\bar{3}1c$	ABAB	[42]	$AgScP_2Se_6$	Trigonal	$P\bar{3}1c$	ABAB	[121]
	$AgErP_2S_6$	–	–	–	–	$AgErP_2Se_6$	Trigonal	$P\bar{3}1c$	ABAB	[121]
	$AgTmP_2S_6$	–	–	–	–	$AgTmP_2Se_6$	Trigonal	$P\bar{3}1c$	ABAB	[121]
	$AgVP_2S_6$	Trigonal	$P\bar{3}1c$	AAA	[122]	$AgVP_2Se_6$	Monoclinic	C2	AAA	[123]
	$AgCrP_2S_6$	–	–	–	–	$AgCrP_2Se_6$	Monoclinic	C2/m	AAA	[119]
	$CuAlP_2S_6$	–	–	–	–	$CuAlP_2Se_6$	Rhombohedral	$R\bar{3}$	ABC	[124]
	$AgAlP_2S_6$	–	–	–	–	$AgAlP_2Se_6$	Monoclinic	C2/m	AAA	[119]
	$CuBiP_2S_6$	–	–	–	–	$CuBiP_2Se_6$	Trigonal	$P\bar{3}1c$	ABAB	[48]
	$AgBiP_2S_6$	–	–	–	–	$AgBiP_2Se_6$	Rhombohedral	$R\bar{3}$	ABCDEF	[48]
	$AgGaP_2S_6$	–	–	–	–	$AgGaP_2Se_6$	Trigonal	$P\bar{3}1c$	ABAB	[119]

[a]The c stacking direction; – denotes data not mentioned in the publications.

behavior. Further refined Wilson–Yoffe model and extended Huckel model[52] were utilized to estimate a band structure. These $M^{II}PS_3$ (M^{II}: first raw series transition metals) compounds possess similar electronic band structures. Some of the known semiconducting MPX_3 compounds have been surveyed and collected in **Table 3**. The value of their bandgaps ranges from 1.3 eV for $FePS_3$ to 3.5 eV for $CdPS_3$.[49] Compared with the bandgaps of sulfides, those of selenides are smaller due to the relative electronegativity of S and Se atoms. It can be seen that the value of the bandgap is closely related to the metal cations present in the compound. Additionally,

in 1996, Zhukov et al.[53] calculated and discussed the relation between the electronic structure and the spin polarization in metal ions. The linear muffin-tin method with the atomic sphere approximation was utilized. The $3d$ regions of the density of state (DOS) of MPS_3, including $MnPS_3$, $FePS_3$, and $NiPS_3$, are displayed in Figure 5b, demonstrating the relative energies of t_{2g} and e_g bands and their occupations with the shaded areas. The spin-up states are more stable with lower energy than the spin-down ones, indicating they are at a high-spin configuration, consistent with the results based on experiments.[18,50]

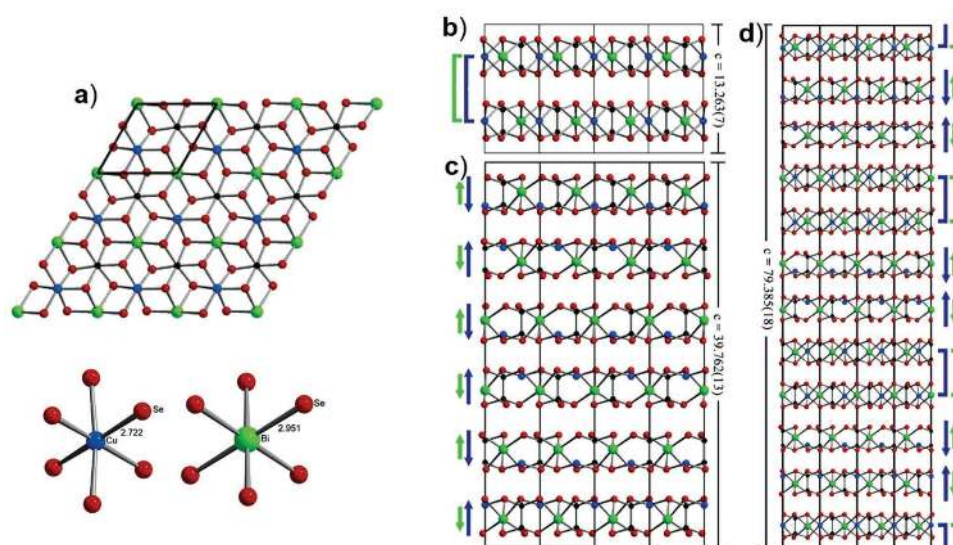**Figure 4.** a) View of a single $CuBiP_2Se_6$ layer down the c-axis [(001) direction] showing the ordered arrangement of the metal ions (top) and the immediate coordination environment of Cu+ and Bi^{3+} in $CuBiP_2Se_6$ at room temperature. b) 298 K, c) 173 K, and d) 97 K structures of $CuBiP_2Se_6$ viewed down the[110] direction. Reproduced with permission.[48] Copyright 2005, American Chemical Society.
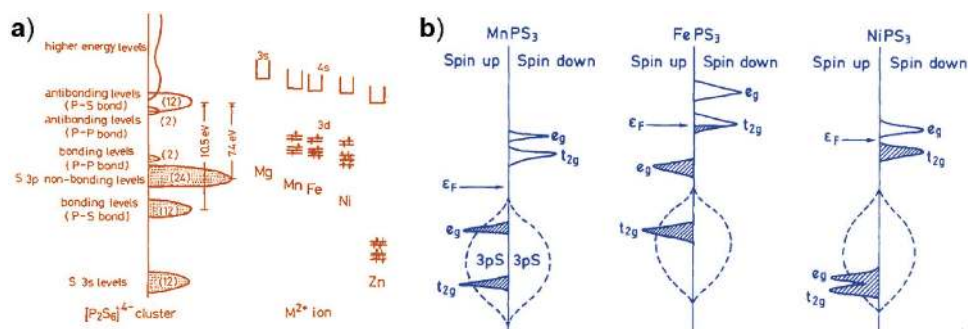
Figure 5. a) Energy level scheme of MPS$_3$. It is constructed from the energy levels of [P$_2$S$_6$]$^{4-}$ clusters and localized divalent metal ions based on the absorption spectra. Reproduced with permission.[50] Copyright 1986, Elsevier B.V. b) 3d region of the DOS of MPS$_3$ showing the relative energies of the spin-polarized t$_{2g}$ and e$_g$ bands and their occupations. Reproduced with permission.[53] Copyright 1996, Elsevier Ltd.

From the perspective of band theory, the orbital projected partial DOS of single-layer MnPS$_3$, FePS$_3$, and NiPS$_3$ are demonstrated in **Figure 6**,[54] revealing that the s and p orbitals of the P atoms mainly contribute to the conduction-band edges, while the top of valence band is significantly contributed by the chalcogen's atomic orbitals. Notably, considering the specific composition and magnetic configuration of these MPX$_3$ materials, the edges of valence band and conduction band are dominated by metal, phosphorus, or chalcogen atoms. The crystal field splitting of the d-orbitals and the filling fractions affect their electronic structures near the Fermi level.[54] The ab initio calculations conducted by Chittari et al.[54] predict that most bandgaps of the anti-ferromagnetic MPX$_3$ crystals decrease with the increase of the atomic number of the chalcogen. Thus, half-metallic structure with ferromagnetic states or nonmagnetic metallic states is properly obtained in some cases.

Regarding other metals, e.g., Mg and Zn based MPX$_3$ structures, their electronic DOS and orbital contribution are somehow different. MgPS$_3$ contains no d electrons. Its valence band consists primarily of S and Mg states, and S and P states dominate its conduction band. While ZnPS$_3$, whose d orbital shell is fully filled, shows the sharply localized 3d-levels below the top of the valence band.[55] Recently, the band diagram for CuInP$_2$S$_6$ was calculated by using density functional theory (DFT)-based ab initio theory to simulate the Jahn–Teller effect, which would make a contribution to the ferroelectric ordering of CuInP$_2$S$_6$.[56]

Table 3. Reported calculated and experimental bandgaps for various MPX$_3$ compounds.

Components	Bandgaps[20]			Experimental	Type
	Calculated				Indirect/Direct
	E$_g$	CBM	VBM		
ZnPS$_3$	3.30^{ML}(HSE06)[93]	−3.34	−6.64	3.5^{B}[20]	Indirect
CdPS$_3$	3.03^{ML}(HSE06)[93]	−3.70	−6.73	3.4^{B}[20]	Indirect
MnPS$_3$	3.05^{ML}(HSE06)[54]	–	–	3.0^{B}[49]	Direct
FePS$_3$	2.54^{ML}(HSE06)[21]	–	–	1.5^{B}[49]	Indirect
NiPS$_3$	3.01^{ML}(HSE06)[21]	–	–	1.6^{B}[49]	Indirect
VPS$_3$	2.50^{ML}(HSE06)[54]	–	–	–	Indirect
CuPS$_3$	1.76^{ML}(HSE06)[54]	–	–	–	Indirect
MgPS$_3$	3.94^{ML}(HSE06)[93]	−3.07	−7.01	–	Direct
CuInP$_2$S$_6$	–	–	–	2.9^{B}[125]	Direct
AgScP$_2$S$_6$	3.16^{ML}(HSE06)[93]	−3.55	−6.71	–	Direct
AgBiP$_2$S$_6$	–	–	–	1.7^{B}[125]	–
AgInP$_2$S$_6$	2.41^{ML}(HSE06)[93]	−3.65	−6.06	–	Indirect
CdPSe$_3$	3.03^{ML}(HSE06)[93]	−3.70	−6.73	2.29^{B}[126]	Indirect
ZnPSe$_3$	2.32^{ML}(HSE06)[93]	−3.71	−6.02	–	Indirect
FePSe$_3$	1.48^{ML}(HSE06)[54]	–	–	1.3^{B}[49]	Indirect
MnPSe$_3$	2.24^{ML}(HSE06)[54]	–	–	2.5^{B}[49]	Direct
VPSe$_3$	2.10^{ML}(HSE06)[54]	–	–	–	Indirect
NiPSe$_3$	2.22^{ML}(HSE06)[21]	–	–	–	Indirect
CuPSe$_3$	0.56^{ML}(HSE06)[54]	–	–	–	Indirect
MgPSe$_3$	2.97^{ML}(HSE06)[93]	−3.38	−6.35	–	Direct
CuBiP$_2$Se$_6$	–	–	–	1.2^{B}[48]	Indirect
AgBiP$_2$Se$_6$	–	–	–	1.4^{B}[48]	–
AgScP$_2$Se$_6$	2.66^{ML}(HSE06)[93]	−3.79	−6.45	1.55^{B}[121]	Direct
AgInP$_2$Se$_6$	1.77^{ML}(HSE06)[93]	−4.03	−5.80	–	Indirect

ML denotes the "monolayer" of MPX$_3$. B denotes the "bulk crystal" of MPX$_3$.

1.2.2. Optical Properties

The research on the optical properties of layered MPX$_3$ crystals started in the early 1880s,[57] Piacentini et al.[57] collected the optical absorption spectra in the energy range 0–5.4 eV for NiPS$_3$ at different temperatures (300, 78, and 4.2 K). The features observed in the spectrum were interpreted to explain the transitions within the different Ni^{2+} 3d levels and transitions between the S 3$p_x p_y$ valence states and the Ni^{2+} 3d empty states (e$_g$ orbital) (Figure 5a). Furthermore, the study about the Raman spectra of
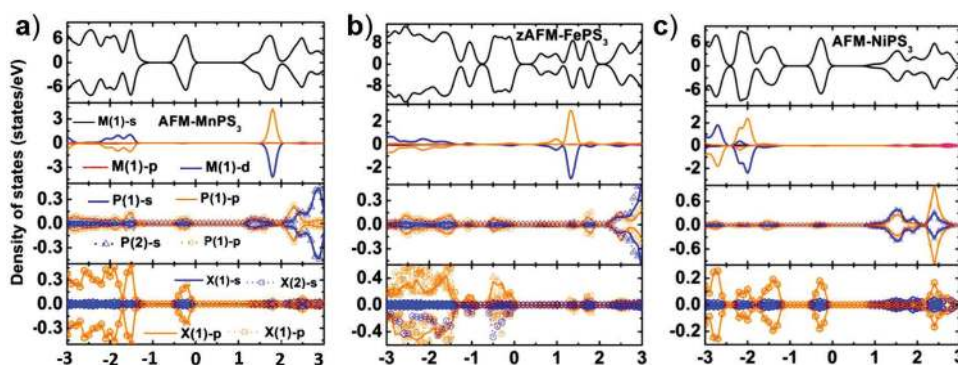
Figure 6. Orbitally projected partial density of the states (PDOS) of a) $MnPS_3$, b) $FePS_3$, and c) $NiPS_3$ calculated for self-consistently converged ground-state magnetic configurations. Reproduced with permission.[54] Copyright 2016, American Physical Society.

various layered 2D materials is a hot topic. As a popular characterization tool, the features present in the Raman spectra are helpful to estimate the thickness of nanosheets, such as graphene and TMDs.[58] Du et al.[20] studied the Raman spectra of $FePS_3$ nanosheets with different thicknesses, revealing the strong interlayer vibrations in three-layered $FePS_3$ and stable structure of monolayer $FePS_3$ under ambient conditions (**Figure 7**a). The comprehensive investigation[59] of the layer-number and temperature dependent Raman spectra shows a magnetic persistence in $FePS_3$ nanosheets with different layers, including single layered $FePS_3$ nanosheet. But the Neel temperature of the anti-ferromagnetic $FePS_3$ sample reduces from 117 K in bulk to 104 K in the monolayer. Some more works[60,61] on the Raman spectroscopic study reveal a similar trend for $NiPS_3$ nanosheet which also exhibits a substantially varying feature depending on the number of layers. A remarkable linear relation is found between the Raman intensity of the peak for A_g mode of $NiPS_3$ on a sapphire substrate and the thickness in Figure 7b,c,[61] which provides a simple way to estimate their thickness.

1.2.3. Magnetism

Recently, the discovery and characterization of magnetism of novel 2D crystals have been a major research direction.[18,62] Ultimately, the magnetic functionality of these 2D materials is employed for fabricating spintronic or magnetoelectronic applications.[63] MPX_3 members, being an important family of layered 2D materials, have potential application in low-dimensional magnetic and spintronic devices.[28,64,65] Until now, experimental studies and theoretical calculations of the magnetic properties of MPX_3 have been widely performed. The experimental studies on magnetic properties were mainly focused on the MPX_3 with bulk crystals,[39,64,66–68] while the theoretical calculations of the spin-state were concentrated on single-layered MPX_3 nanosheets.[21,54] There are three types (**Figure 8**a) of magnetic moments-distributions that were proposed for the MPX_3 crystals[29] in 1900s. In $NiPS_3$ and $CoPS_3$ monolayers, double parallel ferromagnetic chains are anti-ferromagnetically coupled (type I) with each other. For $MnPS_3$ layers, a magnetic ion anti-ferromagnetically coupled with the three nearest neighbors
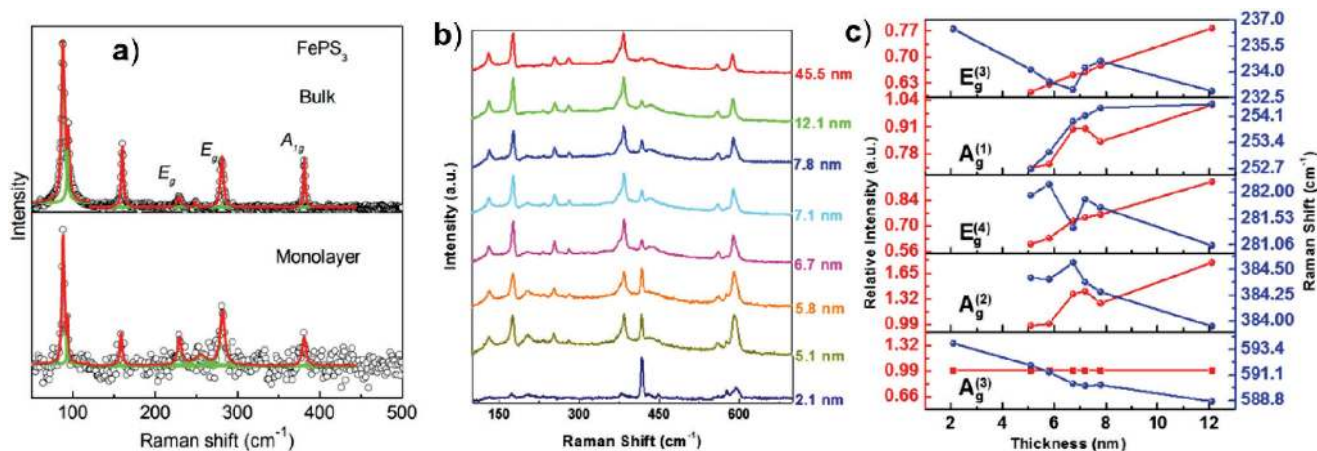
Figure 7. a) Raman spectra of bulk and monolayer $FePS_3$ obtained with a 532 nm laser at ≈77 K. Reproduced with permission.[20] Copyright 2015, American Chemical Society. b) Raman spectra of nanosheets on sapphire substrate with varying thickness from 2.1 to 45.5 nm. c) The thickness dependence of relative intensity (red curve) and Raman shift (blue curve) of selected modes in (b). Reproduced with permission.[61] Copyright, 2017, Wiley-VCH.
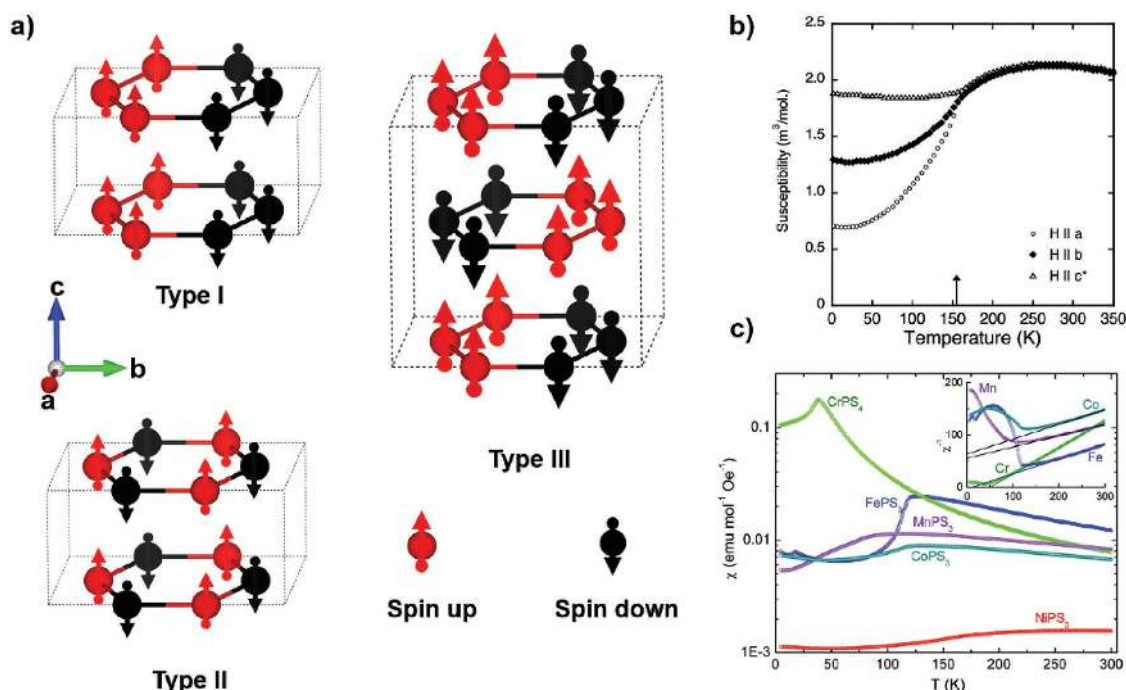
Figure 8. a) The schematic of three published magnetic structures of MPX$_3$. Type I, type II, and type III for NiPS$_3$, MnPS$_3$, and FePS$_3$, respectively. The moments are on the metal sites. b) Examples of the zero-field-cooled magnetic susceptibility of a NiPS$_3$ crystal measured along some high symmetry directions in an applied magnetic field of 0.1 T. The arrow marks the expected Neel temperature of 155 K. Reproduced with permission.[72] Copyright 2015, American Physical Society. c) Magnetic susceptibility of the MnPS$_3$, CoPS$_3$, NiPS$_3$, and FePS$_3$ phases measured at a field of 1000 Oe. The inset is the inverse susceptibility representation (without NiPS$_3$). Reproduced with permission.[66] Copyright 2017, American Chemical Society.

in the layer (type II) and their net magnetic moments pointing vertically to the basal planes. In FePS$_3$, each Fe^{2+} ion is ferromagnetically coupled with two of the three nearest neighbors in single layer. Meanwhile, each plane is anti-ferromagetically coupled to adjacent interplanar ones, which is contrary to the type I structure (type III). Meanwhile, FePS$_3$ has been of interest for its realization of the anti-ferromagnetic 2D Ising model on a honeycomb lattice.[64,69] As temperature decreases across ≈118 K, FePS$_3$ undergoes a conversion from the paramagnetic to the antimagnetic phase.[59] Magnetic measurement shows that bulk Ni, Fe, Mn, and Co based MPS$_3$ or MPSe$_3$ have been found to be anti-ferromagnetic with Neel temperatures (T_N) at a range of 82–155 K.[29,39,70] Additionally, the magnetic properties of the MPX$_3$ crystal are affected by the test conditions and magnetic field intensity. Taking the NiPS$_3$ crystal as an example, some previous results demonstrate[64,71] that the susceptibility was a function of temperature and it was anisotropic above T_N. Conversely, Wildes et al.[72] found that the susceptibility is isotropic above the T_N (T_N = 155 K) while it becomes anisotropic below the T_N with an applied field of 0.1 T along three high symmetry directions, a, b, and c (Figure 8b).

Most bulk MPS$_3$ (M = Ni, Fe, Co, and Mn) compounds are anti-ferromagnetic below their T_N and are paramagnetic above the T_N. As is shown in Figure 8c,[29,66] their magnetic susceptibility was conducted at a field of 1000 Oe. Parameters such as apparent total spin S assuming zero orbital moment, the magnetic moment, Neel temperature, and Weiss constant could be evaluated from the susceptibility data. The Weiss constant of MnPS$_3$ (−245 K), CoPS$_3$ (−223 K), and NiPS$_3$ (−712 K) is

negative while it is a positive value for FePS$_3$ (16 K), indicating the existence of ferromagnetic correlations. However, some compounds, such as CdPS$_3$, ZnPS$_3$, and SnPS$_3$, in this family exhibit diamagnetism under any temperature because of the core electrons. The magnetic parameters of these bulk MPX$_3$ compounds are illustrated in **Table 4**.

The magnetism of the MPX$_3$ crystals in the 2D limit has attracted tremendous attention recently. In this regard, MPX$_3$ monolayers are studied by theoretical calculations except for FePS$_3$ which has an experimental evidence as well. These

Table 4. A list of bulk MPX$_3$ compounds with the known magnetic data.

Compound	Type of magnetism[a]	Neel temperature[b] [K]	Magnetic moment [μB]
NiPS$_3$	AFM[27]	155[27]	3.9[49]
MnPS$_3$	AFM[27]	78[27]	3.1[27]
MnPSe$_3$	AFM[39]	74 ± 2[39]	4.74[27]
FePS$_3$	AFM[39]	118[64]	5.0[27]
FePSe$_3$	AFM[39]	119 ± 1[39]	4.9[27]
CoPS$_3$	AFM[49]	132[49]	–
AgVP$_2$S$_6$	AFM[127]	10–15[127]	–
AgCrP$_2$S$_6$	AFM[128]	20[128]	–
AgCrP$_2$Se$_6$	AFM[79]	42[79]	–
CuCrP$_2$S$_6$	AFM[79]	40[79]	–
CuCrP$_2$Se$_6$	AFM[11]	30[11]	–

[a,b] The experimental data based on bulk MPX$_3$ crystals.

ADVANCED
SCIENCE NEWS
www.advancedsciencenews.com

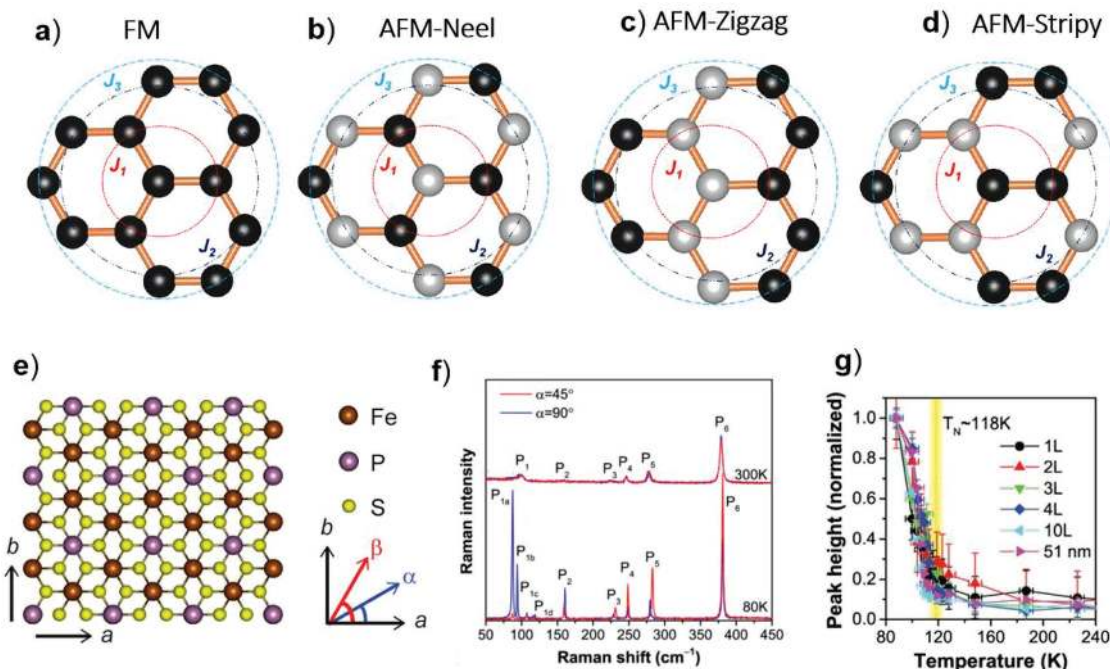ADVANCED
FUNCTIONAL
MATERIALS
www.afm-journal.de

Figure 9. Top view of different magnetic ordering arrangements: a) ferromagnetic, b) Neel anti-ferromagnetic, c) zigzag anti-ferromagnetic, and d) stripy anti-ferromagnetic. The black and white spheres represent up and down spins, respectively. The red circles identify the nearest neighbors (NN) of the central metal site, the navy blue circles (dashed–dotted) identify the second-nearest neighbors, and the light blue circles identify the third-nearest neighbors. (a)–(d) Reproduced with permission.[54] Copyright 2016, American Physical Society. e) $a–b$ plane of monolayer $FePS_3$. Definitions of the incident (α) and scattered (β) polarization angles are shown. f) Polarized Raman spectra of bulk $FePS_3$ at 80 and 300 K in parallel polarization configurations ($\alpha = \beta$), for $\alpha = 45°$ and 90°, respectively. g) Temperature dependence of the P_{1a} peak height at different thicknesses. (e)–(g) Reproduced with permission.[35] Copyright 2016, American Chemical Society.

studies mainly focus on monolayer magnetic ordering, the relationship between band structure and magnetic phase, and modulation techniques. Chittari et al.[54] studied the electronic and magnetic properties of single-layer MPX_3 (M = V, Cr, Mn, Fe, Co, Ni, Cu, and Zn; X = S, Se, Te) via first-principles calculations. For the MPX_3 monolayer, there are four magnetic orderings (illustrated in **Figure 9**a–d) which include ferromagnetism (FM), Neel anti-ferromagnetism (AFM), zigzag AFM (zAFM), and stripy AFM. As to the FM ordering, all the spin-states of the metal atoms have the same orientation. In addition, the spin-states in the nearest neighbor metal atoms have an opposite orientation for the Neel anti-ferromagnetic ordering. The zigzag AFM ordering, where the spin-state of the adjacent metal atom chains along the zigzag direction has an opposite orientation, is different from the previous two. However, the spin-state of the adjacent metal atoms for the stripy anti-ferromagnetic ordering chain along the armchair direction has an opposite orientation. According to the DFT results,[54] monolayers VPX_3, $MnPX_3$, and $NiPX_3$ (X = S, Se, and Te) prefer the AFM ordering, while the nonmagnetic state of monolayer $CoPX_3$, $CuPX_3$, $ZnPX_3$, and $FePX_3$ is more stable than the others, except for $FePS_3$, which prefers the zAFM ordering. Beyond that, monolayers $CrPS_3$ and $CrPSe_3$ are ferromagnetic. Recently, several studies on spin properties using Raman spectroscopy have reported on spin–phonon coupling and quasielastic scattering owing to the difficulty in directly measuring the magnetic behaviors of atomically thin 2D crystals.[59,73] In the Raman spectra of magnetic crystals, the appearance of two magnon scattering and change

of the Raman peak positions or intensities suggest ordered spin states.[35,74] Particularly, the changes in the Raman spectrum of anti-ferromagnetic materials concomitant with a magnetic transition are good signals for monitoring their magnetic ordering. Based on this method, Wang et al.[59] verify the magnetic persistence in monolayer $FePS_3$ nanosheets, revealing that the intralayer spin arrangement dominates the magnetic structure. The $FePS_3$ nanosheets with different layers were studied by monitoring the intensity of the Raman peaks (P_{1a}), which result from zone folding because of AFM ordering at the transition temperature.[35] Lee et al. found that it exhibits an Ising type AFM ordering when its thickness reduces to the monolayer (0.7 nm) (Figure 9e–g). Moreover, the transition temperature ($T_N \approx 118$ K) remains irrelevant to the thickness of $FePS_3$. This result indicates that the weak interlayer interaction plays a negligible role on the anti-ferromagnetic ordering.

Notably, there is a certain correlation between band and magnetic structure of monolayer MPX_3,[54] proved by the first principle calculation. Monolayer MPX_3 nanosheets are generally metallic with ferromagnetic ordering. Particularly, monolayer $CoPX_3$ turned out to be nonmagnetic. The band structures of various monolayer MPX_3 (**Figure 10**a) show that the nonmagnetic ones (with green bands) can be metal (Co-based and Cu-based MPX_3 compounds), semiconductor ($FePX_3$), or insulator ($ZnPX_3$). The semiconducting ones, such as VPX_3, $MnPX_3$, $NiPX_3$, and $FePX_3$, exhibit anti-ferromagnetic ordering, while, Cr-based compounds show ferromagnetic ordering with a metallic phase.
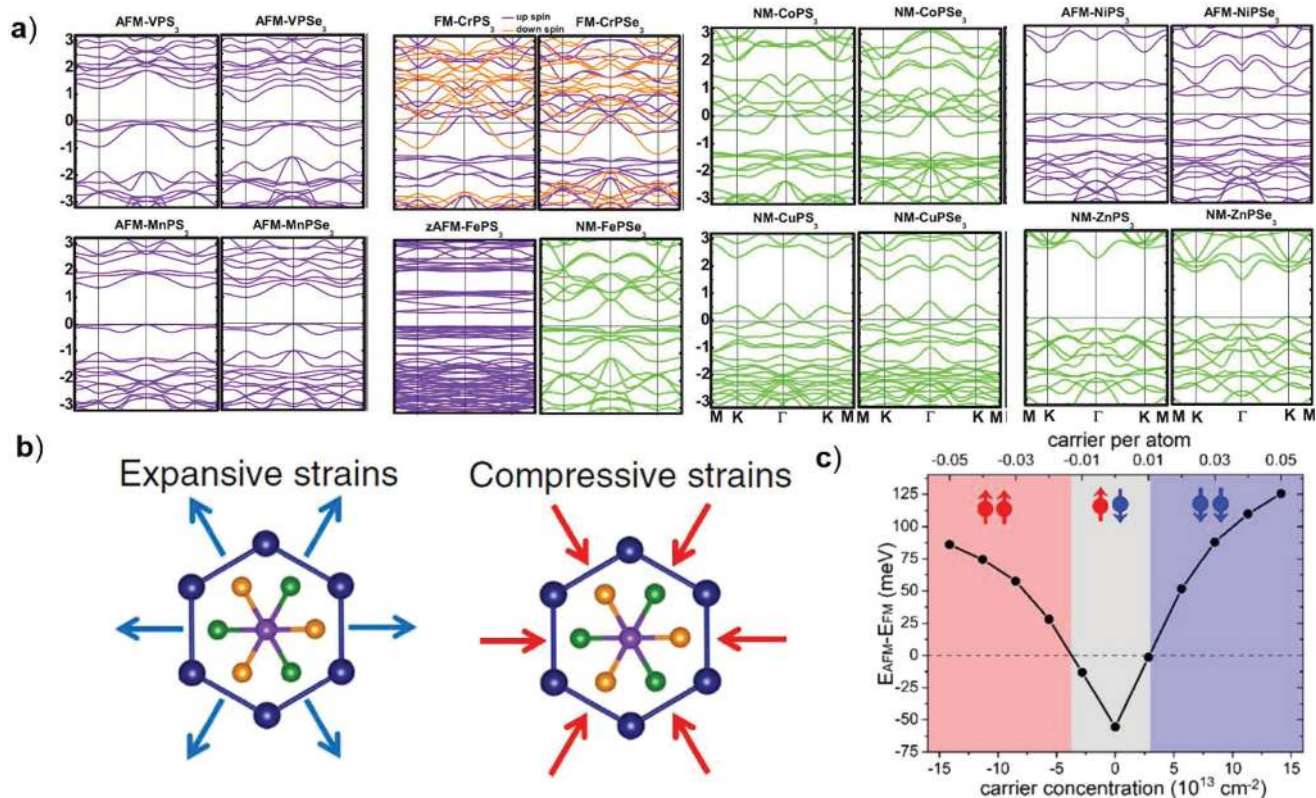
Figure 10. a) Band structures for single-layer MPX$_3$ (M = V, Cr, Mn, Fe, Co, Ni, Cu, and Zn. X = S, Se) compounds in their lowest-energy magnetic configuration. The bands are violet for AFM configurations, violet and orange for the up and down split spin bands in the FM configurations, and green for the NM phases. b) Influence of in-plane strain on the magnetic configurations of selected MPX$_3$ compounds. Reproduced with permission.[54] Copyright 2016, American Physical Society. c) Relative energy of AFM and FM states under the variation of carrier concentration for 2D MnPSe$_3$. The positive and negative values are for electron and hole doping, respectively. The up and down arrows indicate up-spin and down-spin, respectively. Reproduced with permission.[28] Copyright 2014, American Chemical Society.

The magnetic phase transition can also be realized through applying stress or modulating the carrier concentration. Chittari et al.[54] found that applied strains can act as switchers to give rise to transitions or change in the stability of the magnetic phases. The compressive and expansive biaxial strains can be obtained through enlarging rectangular unit cell. Similarly, scaling either in the zigzag or armchair directions is used to obtain the uniaxial strains (Figure 10b). Theoretically, huge strains are required to tune the magnetic behavior of MnPS$_3$. However, for other systems, such as CrPS$_3$, FePS$_3$, FePSe$_3$, and NiPS$_3$, the transitions of magnetic properties can be realized when a small strain is applied. Moreover, Yang and co-workers[28] predicted that controlling the carrier concentration will lead to a magnetic phase transition from the AFM phase at the ground state to the FM phase after the observation is made via increasing the density of the carriers (1.4×10^{14} cm^{-2}) on the MnPSe$_3$ nanosheet (Figure 10c).

Alloying is also an approach to alter the magnetic properties for these MPX$_3$ materials. The nonmagnetic metal element (Mn) is alloyed with ZnPS$_3$ to obtain the Mn$_x$Zn$_{1-x}$PS$_3$ crystal.[75] The alloying extent, namely, the value of x, usually has an influence on the value of T_N and the magnetic phase of the alloyed MPX$_3$. The study of the Mn$_x$Zn$_{1-x}$P$_1$S$_3$[75] crystal demonstrates that its T_N value is related to the concentration of Zn atoms. It decreases concomitantly when the concentration

of the nonmagnetic cation species increases. A T_N/applied-field(Hz)/dilution magnetic phase diagram for Mn$_x$Zn$_{1-x}$P$_2$S$_6$ is shown in **Figure 11**a. In this diagram, the enclosed region is the AFM region with a percolation threshold of $x = 0.7$. A high-order paramagnetic phase and a disordered paramagnetic phase will appear with a large magnetic field and high temperature, respectively. Likewise, the low percentage ($x < 0.7$) of Mn atoms also introduces the paramagnetic phase. Above the top surface of the AFM region, the spin-flop phase dominates the diagram. The other is alloying MPX$_3$ with magnetic metal for Mn$_{1-x}$Fe$_x$PS$_3$[76] and Fe$_{0.5}$Ni$_{0.5}$PS$_3$.[68] The substitutive magnetic metal atom, like Mn and Fe atoms, in alloyed MPX$_3$ is more likely to bring about a magnetic glass phase or a spin glass phase. The alloyed Mn$_{1-x}$Fe$_x$PS$_3$ exhibits a spin glass state when a portion of the Mn atoms are substituted by other magnetic Fe atoms (Figure 11b).[76] It is clear that the magnetic phase of Mn$_{1-x}$Fe$_x$PS$_3$ changes with the increase of the iron concentration. Obviously, the anti-ferromagnetic phases exist in the ranges of $0.0 \leq x \leq 0.2$ and $0.8 \leq x \leq 1.0$. The spin glass state is in the range of $0.5 \leq x \leq 0.6$ and the reentrant spin glass state is confined to the ranges of $0.3 \leq x \leq 0.45$ or $0.6 \leq x \leq 0.7$ at a low temperature. Apart from the spin glass state, a magnetic glass state may appear in a magnetically substituted MPX$_3$ system. Goossens et al.[68] found that this alloyed system shows obvious hysteresis for Fe$_{0.5}$Ni$_{0.5}$PS$_3$ in the transition temperature and
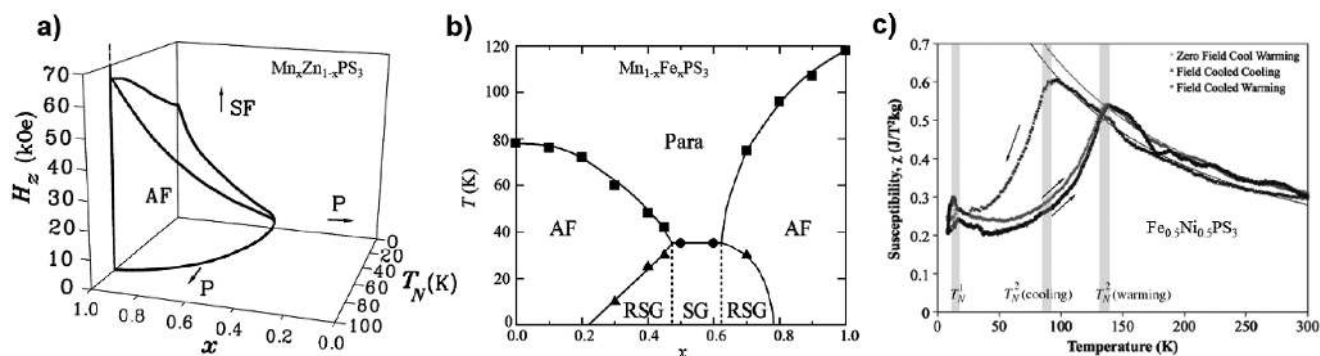
Figure 11. a) The temperature/applied-field(H = H_Z)/dilution phase diagram for $Mn_xZn_{1-x}PS_3$. SF, AF, and P stand for the spin-flop, anti-ferromagnetic, and paramagnetic phases, respectively. Reproduced with permission.[75] Copyright 1998, IOP Publishing. b) Magnetic phase diagram of the $Mn_{1-x}Fe_xPS_3$. The notations SG, RSG, AF, and Para show a spin glass, a re-entrant spin glass, an anti-ferromagnetic ordered, and a paramagnetic phase, respectively. Reproduced with permission.[76] Copyright 2007, Elsevier B.V. c) Magnetic susceptibility of a $Fe_{0.5}Ni_{0.5}PS_3$ powder, measured in a field of 1 T under a range of conditions. The directions of temperature change were as follows: (1) warming after cooling in the zero field (ZFCW); (2) cooling in a field (FCC); and finally (3) warming after cooling in a field (FCW). Reproduced with permission.[68] Copyright 2013, Elsevier B.V.

also related to the direction of temperature change (Figure 11c). Two Neel temperatures of 14 and 97 K or ≈138 K, referring to T^1_N and T^2_N, were found, and three magnetic phases could be distinguished from the measured susceptibility of $Fe_{0.5}Ni_{0.5}PS_3$. Meanwhile, there is a distinct thermal hysteresis in the field cooled cooling (FCC) and field cooled warming (FCW) susceptibilities. The FCC state also transforms into zero field cooled warming (ZFCW)/FCW states after relaxation over a period of ≈2 h. These results reveal the existence of magnetic glass.[68]

1.2.4. Ferroelectricity

One of the interesting phenomena in metal thiophosphates or selenophosphates is the presence of ferroelectric ordering.[44,77,78] Usually, the ferroelectric ordering only appears on $M_IM_{II}P_2X_6$ crystals, such as $CuInP_2S_6$,[44] $CuInP_2Se_6$,[79] $CuBiP_2Se_6$,[48] and $AgBiP_2Se_6$.[48] A list of all $M_IM_{II}P_2X_6$ compounds and their ferroic ordering is illustrated in **Table 5**. Especially, the ferroelectric ordering of $CuInP_2S_6$ has been widely studied. The structure of $CuInP_2S_6$ is shown in **Figure 12**a. Cu^I atoms can move among three sites, as follows: the first site is closest to the center of the octahedron (Cu1), the second site is further off-center (Cu2), and the third site is in the interlayer space (Cu3).[80] The transition from order to disorder occurs at 315 K[44] with indirect evidence for copper hopping motions. Above the temperature of 315 K, the symmetry of the $CuInP_2S_6$ phase is apparent because the first site has two positions, i.e., "up" and "down" positions

(Figure 12b), and the third site shows an equal position of both "up" and "down".[44] When the $CuInP_2S_6$ is cooled below 315 K(Figure 12c), the motion of the intersite Cu is restricted to lock the Cu^{1+} sublattice in the "up" position with a compensatory shift of the In^{3+} sublattice to the opposite polarity, leading to the formation of a non-centrosymmetric ferroelectric phase. An obvious symmetry transition is from the paraelectric phase to the ferroelectric phase when the temperature is 315 K. Additionally, small amounts of element substitution either of the In or S site will lead to intriguing regulation in the nature properties. If the Se content is increased in $CuInP_2(S_xSe_{1-x})_6$, the regulation from ferroelectric to a dipolar glass or other phase is easily triggered.[77] Similarly, the $CuVP_2S_6$ crystal is also found to exhibit ordered displacement of metal ions at a low temperature. The Cu^I in the trigonal site forming acentric C2 symmetry will be frozen below 20 K.[81]

In addition, hydrostatic pressure is also applied to realize the structural phase transition of $CuInP_2S_6$. Its ferroelectric transition temperature (T_c), demonstrating the linear increment along with the strength of pressure ($\partial T_c/\partial P$ = 210 K GPa^{-1}), can be tuned with pressure.[82] This result indicates the transition from order to disorder nature and the coupling effect of ferroelectric dipoles across the vdW gap. Notably, the ferroelectric polarization can occur in $CuInP_2S_6$ crystal when the temperature is above the room temperature. This is unique for the vdW layered crystals. The domain structure, switchable polarization, and hysteresis loops in the ambient and ultrahigh vacuum scanning probe microscopy spectra, studied by Belianinov et al.,[83] directly reveal stable, ferroelectric polarization of this crystal. They also found that the domain structure of flakes, whose thickness is >100 nm, is similar to the cleaved bulk surfaces, whereas polarization disappears when its thickness is below 50 nm, which is originated from the instability of polarization under the depolarization field. The piezoresponse force microscopy studies show that the polarization switching at high bias is also related to the ionic mobility and the ferroelectric domains are persistent across several hundreds of layers.[83,84] The ferroelectric properties are also shown in the $MPSe_3$ class. The P_2Se_6 bond possesses a weaker degree of covalence than that in P_2S_6 bonds. Thus, the Cu^I ion displacement occurs at the lower

Table 5. A list of $M^IM^{III}P_2X_6$ compounds with known ferroic ordering.

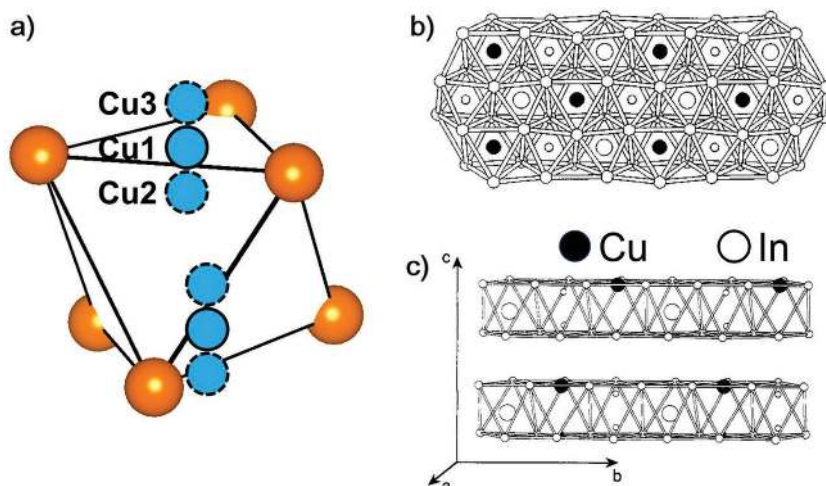| Compound	Ferroically ordered type	Ordering temperature [T_c, K]	Ref.
$CuCrP_2S_6$	Anti-ferrielectric	150	[17]
$CuInP_2S_6$	Ferrielectric	315	[19]
$CuInP_2Se_6$	Ferrielectric	236	[79]
$CuVP_2S_6$	–	20	[81]
$CuBiP_2Se_6$	Anti-ferrielectric	$93 < T_c < 173$	[48]
$AgBiP_2Se_6$	Anti-ferrielectric	$T_c < 295$	[48]

Figure 12. a) The position of three "up" copper sites labeled Cu^1 (the off-center), Cu^2 (the almost central), Cu^3 (the interlayer site). The corresponding "down" sites are also shown. b) Projection onto the a–b plane of the $CuInP_2S_6$ structure showing the triangular sublattices formed by the copper and indium cations and the P—P pairs. c) Two layers of $CuInP_2S_6$ shown in the ferroelectric phase ($T < 315$ K). The up (down) shifted Cu^I (In^{III}) ions are represented by the larger black (white) ball, and the smaller white circles are the P. (a)–(c) Reproduced with permission.[44] Copyright 1997, American Physical Society.

temperature phase.[44,79] Phase transitions in the $CuInP_2Se_6$ compound contain a second-order phase transition at 248 K (T_i) and a first order transition at 236 K (T_c), which is lower than that ($T_c = 315$ K) in $CuInP_2S_6$.[44]

1.2.5. Intercalation Effect

Intercalation is a reversible chemical process to insert foreign species, including molecules and ions, into the crystal gap. The remarkably wide van der Waals gaps existing in MPX_3 compounds create a suitable platform for practical realization of intercalation chemistry. For instance, alkali metals are shown to chemically and electrochemically intercalate into the MPX_3 crystals.[85] Among them, $NiPS_3$, $FePS_3$, and $CoPS_3$ can easily react with butyl-lithium, whereas $CdPS_3$, $ZnPS_3$, and $MnPS_3$ do not. Considering the structure of MPS_3 crystals, filling of all the octahedral sites in the vdW gaps by the lithium cations should lead to the formation of product $Li_{1.5}MPS_3$ (i.e., $Li_3M_2P_2S_6$). At the same time, their magnetic, optical, and electrical properties after lithium intercalation were investigated in detail.[49] The intercalation can result in the occurrence of negative free carriers and a decrement of magnetic susceptibility in Li_xNiPS_3. In addition to these fundamental interests, they can be used in lithium batteries.[23,86] A high formation energy, which is related to the difference between the Li^+/Li potential and the accepting d level, for the intercalation trigger, a high potential of the host compound.[87,88] Thus, the nickel phase was proved to be best candidate used in Li batteries. On the one hand, the ideal size of vdW gap presents the appropriate space to accommodate the Li^+ ions without expansion. The unchanged cell volume is a strong advantage of the MPS_3 materials used as a cathode. On the other hand, the chemistry of MPX_3 compounds has an ionic nature and, hence, they can be viewed as ionic salts with

the metal ions being connecting together by $[P_2S_6]^{4-}$ bridging ligands.[29] Therefore, the high mobility of the metal cations in the ion-exchange mechanism describes the intercalation.

2. Synthesis Methods

The fundamental exploration of functional materials with respect to their properties and applications greatly depends on the development of facile and reliable synthesis methods. Particularly, regarding the case of 2D layered materials, the achievement of an atomic thickness with a lateral size of up to micrometers is sought to realize the interesting properties, especially the unique magnetic and electronic properties. Historically, the attempt to synthesize MPX_3 materials can be traced back to the late 19th century, which was reported by Friedel[17] who obtained $FePS_3$ by heating a weighed amount of phosphorus pentasulfide with iron. Later, Ferrand[19] was then able to extend this technique for growing $ZnPS_3$, $CdPS_3$, and $NiPS_3$ materials. Though investigation of MPX_3 was held back till the introduction of the vapor growth method by Klingen et al. in the mid1960s.[89] Yet, the obtained products using the vapor phase or hydrothermal growth methods[90] had micro size. Very recently, techniques such as chemical vapor deposition and exfoliation were introduced in which ultrathin materials of this family were communicated with interesting applications. In the subsequent section, we present the strategies and progress made for growing MPX_3 materials.

2.1. Exfoliation and Intercalation

Micromechanical cleavage is usually used in fabricating ultrathin nanosheets by exfoliating layered bulk crystals by using Scoch tape or force-assisted liquid exfoliation.[60,91,92] In this regard, the cleavage energies of layered MPX_3 and the formation energies of single-layer MPX_3 are essential properties that need to be considered. Du et al. and Liu et al.[20,93] have calculated the cleavage and the formation energies of some 2D layered MPX_3 materials, respectively. The cleavage energies have been calculated by determining the separation beteween the fractured layer (d) and the original layer (d_0). As shown in **Figure 13**a, the trend of increasing cleavage energy is associated with the enlargment of the interlayer separation and ultimately reaches the maximum level. Of note, the cleavage energy of these layerd MPX_3 materials, except for $FePS_3$, is smaller than that of graphite (≈ 0.36 J m^{-2}),[28] indicating the suitability of layerd MPX_3 materials for exfoliation (Figure 13b). Additionally, the formation energy of layered MPX_3 material is much lower than that of a single-layer MoS_2 (≈ 0.14 J m^{-2}), that is to say, less formation energy is needed in the process of exfoliation from the bulk materials to single-layer nanosheets (Figure 13c).
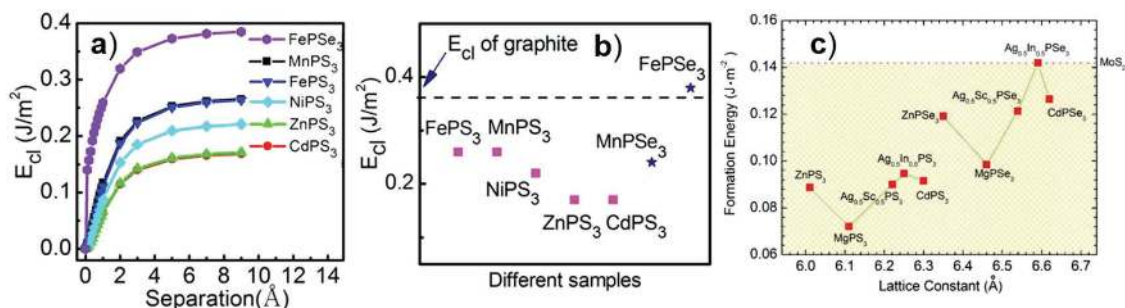
Figure 13. a) Cleavage energy versus the separation distance. b) Comparison of the saturated cleavage energy between graphite and the compounds MPS_3 (pink squares) and $MPSe_3$ (blue stars). Reproduced with permission.[20] Copyright 2015, American Chemical Society. c) Calculated formation energies of single-layer MPX_3 as a functional of the corresponding lattice constants (Å), compared with that of MoS_2. The blue dashed line indicates the formation energy of MoS_2. Reproduced with permission.[93] Copyright 2014, AIP Publishing LLC.

Therefore, both the small values of cleavage and formation energies of layerd MPX_3 materials determine the success in exfoliation of bulk MPX_3 crystals to single layered ones.

The successful preparation of graphene by the "Scotch Tape" method[91] has prompted researchers to comprehensively study lots of layered materials. Inspired by this, the micromechanical cleavage technique has been widely utilized to obtain various types of ultrathin nanosheets from the corresponding layered bulk crystals, including TMD (e.g., MoS_2, WS_2, $MoSe_2$, WSe_2, etc.),[94] MPX_3 (e.g., $MnPS_3$, $FePS_3$, $NiPS_3$, etc.),[20,21,54,95] topological insulators (e.g., Bi_2Se_3, Bi_2Te_3, Sb_2Te_3, etc.),[96] antimonene,[97] and h-BN.[98] Among the 2D materials preparation routes, this method can be regarded as a nondestructive technique due to the mere physical phenomena (no chemical reaction) occurring during exfoliation. Therefore, successfully exfoliated 2D materials exhibit a clean surface, maintaining the "perfect" crystal quality with little defect site. Moreover, the exfoliations can be made in such a way that the lateral size of the obtained material can be up to dozens of micrometers. Recently, the micromechanical exfoliations of MPX_3 materials have been widely reported. As shown in **Figure 14**a,b,

Du et al.[20,93] successfully exfoliated bulk $FePS_3$ crystal to few-layered nanosheets by the "cotch Tape" method. This result can be further confirmed with an optical microscopy photograph and the corresponding AFM topography (Figure 14c,d). Unfortunately, the production yield from micromechanical cleavage technique is quite low with inferior precision and there is restricted controllability for practical application. Additionally, liquid exfoliation has been widely adopted to produce MPX_3 nanosheets. Typically, it requires the addition of some small molecules, such as acetone, lithium ions, and surfactants,[99–101] to assist the process of exfoliation. These types of molecules are able to percolate into the interlayer matrix to expand the van der Waals gaps. Figure 14e depicts a schematic illustration of the small molecule assisted liquid exfoliation of MPX_3 bulk crystals. The scanning electron microscopy (SEM) image of $FePS_3$ bulk crystals and exfoliated $FePS_3$ nanosheets (Figure 14f,g) corroborate the thinning effect of solvent exfoliation.[102] However, impurities and more defective edge sites would be introduced into the MPX_3 nanosheets. This method is not an optimal one for fabricating (photo)electronic devices based on MPX_3 semiconductors where impurities and defects are detrimental for realizing of excellent
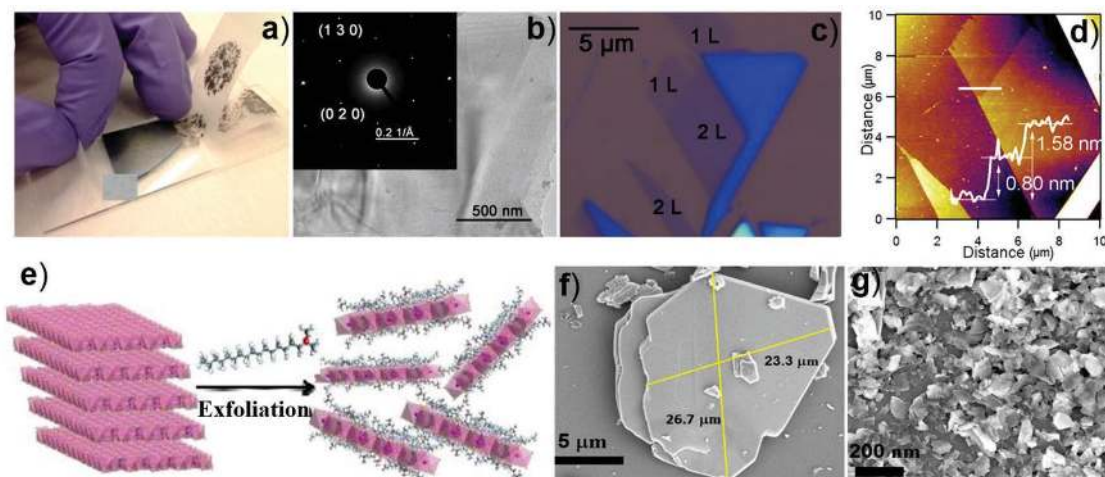

Figure 14. a) Schematic illustration of the typical process with Scotch tape. Reproduced with permission.[129] Copyright 2015, American Chemical Society. b) TEM image and SAED pattern of $FePS_3$. c,d) Optical microscopy photograph and the corresponding AFM topography of $FePS_3$. Reproduced with permission.[20] Copyright 2015, American Chemical Society. e) Schematic illustration of liquid exfoliation of MPX_3 bulk crystals. f,g) SEM image of $FePS_3$ bulk crystals and exfoliated $FePS_3$ nanosheets. Reproduced with permission.[102] Copyright 2016, American Chemical Society.

**ADVANCED
SCIENCE NEWS**

www.advancedsciencenews.com

**ADVANCED
FUNCTIONAL
MATERIALS**

www.afm-journal.de

performance. In the field of catalysts, the controllable introduction of impurities and defect sites are believed to enhance the catalytic activity. It, therefore, appears reasonable to suggest that if high yield fabrication of the catalyst via solvent exfoliation is assured, it may lead to excellent catalytic activity.

2.2. Chemical Vapor Growth

A vast majority of MPX$_3$ compounds with large enough crystals to enable adequate physical characterizations were synthesized through a vapor phase growth technique, i.e., chemical vapor transport (CVT). Stoichiometric amounts of sources, including metal, chalcogen, and phosphorus powders, are located in quartz ampoule along with a transport agent (e.g., iodine) and heated at certain temperature required for the formation of the desired MPX$_3$.[103] The ampoule is made in such a way that it could host a temperature gradient system, such as T1 and T2 (T1 < T2), as shown in **Figure 15**a. In the hotter region (T2), the precursors form vapors to be transported to the cooler region (T1) for undergoing reaction. The temperature of the cooler region should be thermodynamically efficient for making the growth of MPX$_3$ possible, thereby forming a large plate of crystals (Figure 15b). The heating rate is an important parameter in CVT to widen the interlayer distances and control how well the crystallinity is ordered. Ismail et al.[104] adopted the heating rates of 1 and 40 °C min^{-1} to grow FePS$_3$ at 650 °C through the CVT. It was found that a slow heating rate is useful to get the FePS$_3$ with single crystalline phase while the fast heating rate was not. Thus, the slow heating rate induces better

crystallinity. As seen from the scanning electron microscopic image (Figure 15c–f), this technique generally gives bulk materials with compact layers of irregular thicknesses. A comprehensive investigation of layered metal phosphorus trisulfides/selenides was recently made by Pumera and co-workers.[66,105] It can be seen that the growth of different members (with varying the metal or the chalcogen) in the MPX$_3$ family requires separate optimization of the temperature and heating rate. Figure 15g depicts the Raman spectra as a confirmation tool for the formation of the desired product through the CVT method with appropriate heating rates. The CVT grown MPS$_3$ phases are featured by prominent Raman modes from P$_2$S$_6$ units with D3d symmetry (3A1g and 5Eg Raman active modes). In some cases, a pregrown metal oxide/hydroxide precursor is used as a metal source, which is then mixed with a stoichiometric amount of phosphorus and slight in excess of chalcogen in a quartz ampoule. Liang et al.[23] made use of this method to grow FePS$_3$, CoPS$_3$, and NiPS$_3$. The corresponding precursors of metal hydroxide nanosheets were first synthesized via the hydrothermal method then eventually converted to the MPX$_3$ form at 520 °C after being mixed with red phosphorus and sulfur powders. Accordingly, the products of FePS$_3$, CoPS$_3$, and NiPS$_3$ with high crystalline nanosheets, having average thickness and lateral sizes of ≈18 and ≈200 nm, respectively, were obtained. The main drawback of CVT is the long duration of the synthesis process. This can be associated with the slow heterogeneous chemical reaction between the metal, chalcogen, and phosphorus atoms. If exactly the stoichiometric amount is taken at the initial stage, the formation kinetics for MPX$_3$ slows down when the pressure of the gaseous product becomes slow.
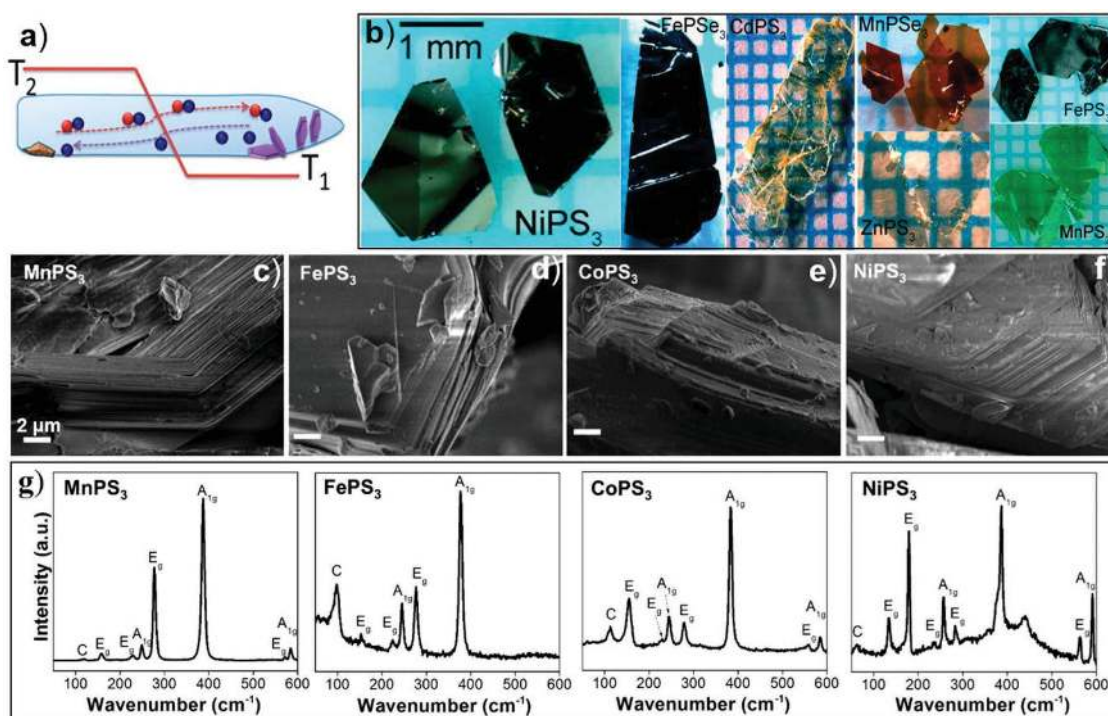

Figure 15. a) Schematics of typical chemical vapor transport (CVT) set-up. b) Photos of bulk 2D crystals obtained via the CVT method. Reproduced with permission.[20] Copyright 2016, American chemical society. c–f) SEM images and g) Raman spectra of various samples grown via the CVT method. Reproduced with permission.[66] Copyright 2017, American chemical society.
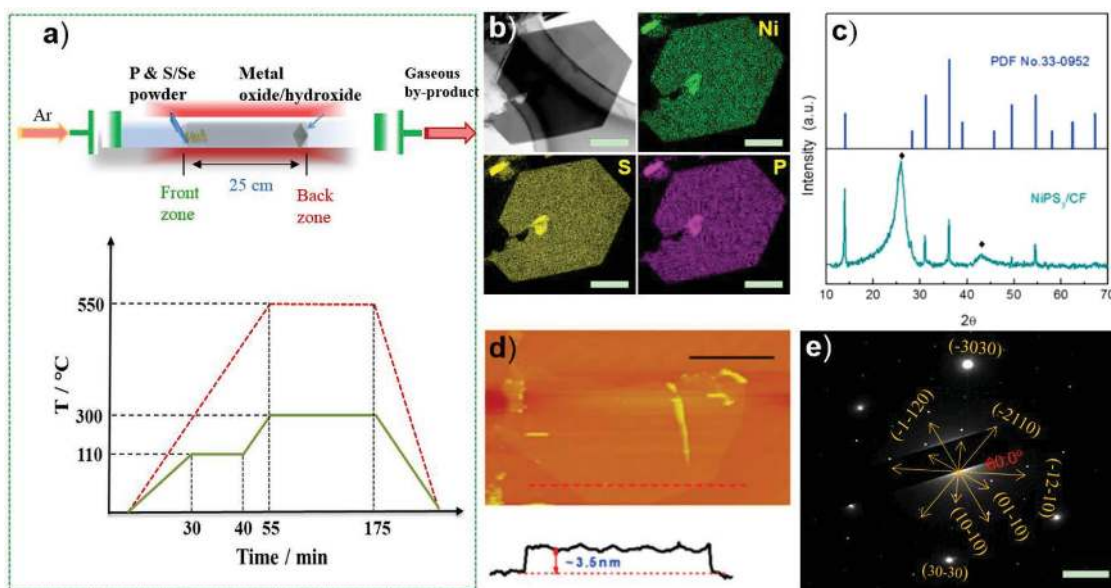
Figure 16. a) Schematics of typical two zone chemical vapor deposition setup (top) and temperature profile in which a preheating strategy is implemented (bottom). b) EDX elemental mapping, c) XRD pattern, and d) AFM image of ultrathin $NiPS_3$ grown according to the schematic shown in (a). e) Selected area electron diffraction pattern of hexagonal $MnPSe_3$ nanosheet grown by a preheating strategy. Scale bars: (b) = 500 nm, (d) = 5 μm, (e) = 2 nm^{-1}. (b)–(d) Reproduced with permission.[36] Copyright 2017, Elsevier. (a),(e) Reproduced with permission.[106] Copyright 2018, Wiley-VCH.

The equilibrium condition for the product dissociation can also be reached, which limits the practical completion of the reaction. Thus, merely raising the temperature cannot lead to a faster growth route.

A more strategic approach in vapor phase growth is the chemical vapor deposition (CVD) method, in which the chemical constituents first heated to vapor phase and then reacted. The desired product is obtained through controlled reaction of one or more volatile precursors on the surface of suitable substrate. In this situation, volatile by-products are also frequently formed and they can be removed by flowing gas in the reaction, chamber as shown in **Figure 16**a (top). As far as the growth of MPX_3 materials is concerned, CVD is a very recent technique that enabled the controllable synthesis for various members to fit to the desired applications. A pregrown metal oxide/hydroxide precursor as a metal source is placed at the back zone to meet the incoming vapors of phosphorus and chalcogen from the front zone. The temperature in the front zone requires careful optimization to assure simultaneous vaporization of both P and S/Se sources, which otherwise results in the introduction of impure phases. The temperature is held constant for ≈10 min, as shown in Figure 16a (bottom), for this purpose. Very recently, He and co-workers reported the synthesis of ultrathin $NiPS_3$ nanosheets on a carbon fiber substrate from $Ni(OH)_2$ nanosheets, red phosphorous, and sulfur using this approach.[36] Reaction time and temperature play substantial roles in tuning the morphology of the incoming product. Initially, small and irregular sheets with sizes below 500 nm were formed. With the increasing of the reaction time, the product increased in lateral size and the nanosheets were formed. Moreover, the low temperature (below 400 °C) was found to be inefficient to complete the reaction and, hence, ruminants of unreacted hydroxides were observed, whereas a high temperature (above 500 °C) caused etching on the surface of the nanosheet. Given the optimized temperature and time of reaction, the obtained nanosheet has the thickness of ≤3.5 nm with the lateral size of larger than 15 μm. And all the elements (Ni, P, and S) distributed uniformly throughout the material (Figure 16b,d). It is also obvious that the X-ray diffraction peaks match the standard $NiPS_3$ crystallographic pattern, as is depicted in Figure 16c. Using this approach, the independent growth of metal chalcogenide may occur along with the growth of the desired MPX_3, in some cases. This problem introduces impure phases and defies the realization of controllable growth. A preheating strategy, which assures the formation of fused mixture of chalcogen and phosphorous, can tackle this problem. After preheating, the mixed vapor can subsequently be carried to the back zone to meet the metal precursors, as depicted in the temperature profile of the growth route (Figure 16a, bottom). The growth made through this approach yielded high crystal quality of $MnPSe_3$ and $MnPS_3$ nanosheets (Figure 16f).[106] Thus, careful optimization of the temperature profile in CVD confers a facile and successful conversion of oxide/hydroxide precursor to phospho-trichalcogenide with phase purity and high crystal quality.

3. Potential Applications of MPX_3 Compounds

3.1. Catalysis

The MPX_3 materials have received significant attention because of their unique physical and chemical characteristics, which are mainly originated from their energy band model and electronic structure. This peculiar structure endows the MPX_3 materials with excellent magnetic, electronic, optical, and catalytic
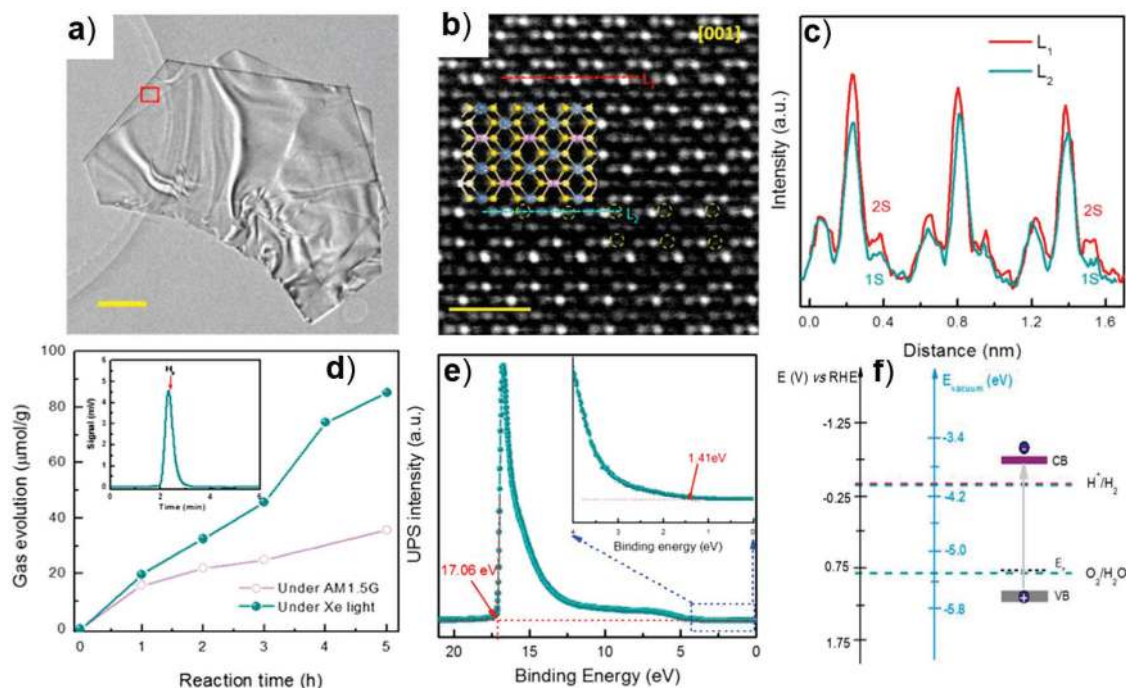
**ADVANCED
SCIENCE NEWS**
www.advancedsciencenews.com

**ADVANCED
FUNCTIONAL
MATERIALS**
www.afm-journal.de

Figure 17. a) Low-magnification TEM image of a hexagonal 2D $NiPS_3$ crystal. b) Atomic-level HAADF-STEM image of an ultrathin $NiPS_3$ nanosheet showing the sulfur vacancies (yellow circles). c) Intensity profiles along lines L1–L2. Higher contract is obtained from the Ni atom compared to the S atom. d) The comparison of H_2 production from pure water under different light irradiation. Inset: A typical gas chromatogram (GC) trace of evolved hydrogen gas after 10 h with irradiation of Xe-Light. e) UPS spectra of $NiPS_3$ crystals. f) Band structure diagram for $NiPS_3$ nanosheets. VB: valence band. CB: conduction band. Scale bar, (a) 1 µm, (b) 1 nm. Reproduced with permission.[36] Copyright 2017, Elsevier Ltd.

properties.[21,30,107] The wide bandgaps (1.3–3.5 eV) and super colossal specific surface area of MPX_3 materials can result in the wide spectrum light absorption, outstanding interfacial reaction activity in photoelectronic properties, and photocatalytic activities. Considering these fascinating properties, the attention of different research groups has been devoted to the rational design of photo (electro) catalysts based on MPX_3 compounds. The experimental realization for photo-electrochemical property of $SnPS_3$, $FePS_3$, and $NiPS_3$ was made in early 1980s on their bulk states.[25,108] Recently, Wang et al. successfully synthesized high crystalline quality 2D structured $NiPS_3$ nanosheets with thickness of a few atomic layers and large lateral sizes up to tens of micrometers (**Figures** 16b–d and 17a–c).[36] The atom resolved high angle annular dark-field scanning transmission electron microscopy (HAADF-STEM) image shows that sulfur vacancies (7.6%) are observed in favor of creating more defective catalytic sites. Interestingly, the $NiPS_3$ nanosheets can realize water-splitting without sacrificial agent to produce hydrogen gas. In this system, the H_2 evolution rates are ≈26.42 and 6.46 µmol g^{-1} h^{-1} under Xe light and simulated solar light, respectively (Figure 17d). Furthermore, a proper bandgap is of primary importance for photocatalytic reactions. Based on the optical absorption spectrum, Mott–Schottky plots, and ultraviolet photoelectron spectroscopy, the conduction band energy (−5.57 eV vs E_{vacuum}) of the $NiPS_3$ nanosheets is placed above the water reduction (H_2/ H_2O) potential (Figure 17e), which is in a thermodynamically efficient position to generate H_2 gas from water. The valence band energy (−3.61 eV) is slightly below the oxidation level of H_2O to

O_2 and the presence of sulfur vacancies will suppress the generation of O_2 gas via forming strong adsorption with an oxygen intermediate species (Figure 17f). These intermediates can be traced by a spin trapping experiment based on electron spin resonance spectroscopy, which detects the surface hydroxyl radicals.[106] This finding reveals that photogenerated holes would oxidize the H_2O molecules adsorbed on the surface of the photocatalysts to hydroxyl radicals, and the road to O−O covalent bond formation for oxygen molecules has not been completed. Thus, much more research on the photocatalytic properties of MPX_3 nanosheets should be conducted to realize the overall water splitting activity with excellent performance.

2D MPX_3 materials are also utilized as electrocatalysts in hydrogen evolution reaction (HER), oxygen evolution reaction (OER), and oxygen reduction reaction, presently.[66,100,105] Their electocatalytic activity results from the appreciable conductivity and abundant active sites at room temperature.[99,105] More significantly, the atomic-level thickness of the MPX_3 materials not only enlarges the specific surface area to expose more active sites but also increases the intrinsic catalytic activity. Song et al.[105] synthesized the bulk materials and corresponding 2D ultrathin nanosheets of $Ni_{1-x}Fe_xPS_3$ (x = 0, 0.05, 0.1, 0.15, 1) via ultrasonication-assisted exfoliation. The SEM and transmission electron microscopy (TEM) images of exfoliated $Ni_{0.9}Fe_{0.1}PS_3$ nanosheets show several micrometers in the lateral size and clear lattice fringes (**Figure 18**a–c). The average thickness of the exfoliated $Ni_{0.9}Fe_{0.1}PS_3$ nanosheets is found to be 4 nm (Figure 18d), indicating that a single nanosheet consists of approximately five layers. The electrochemical tests show that
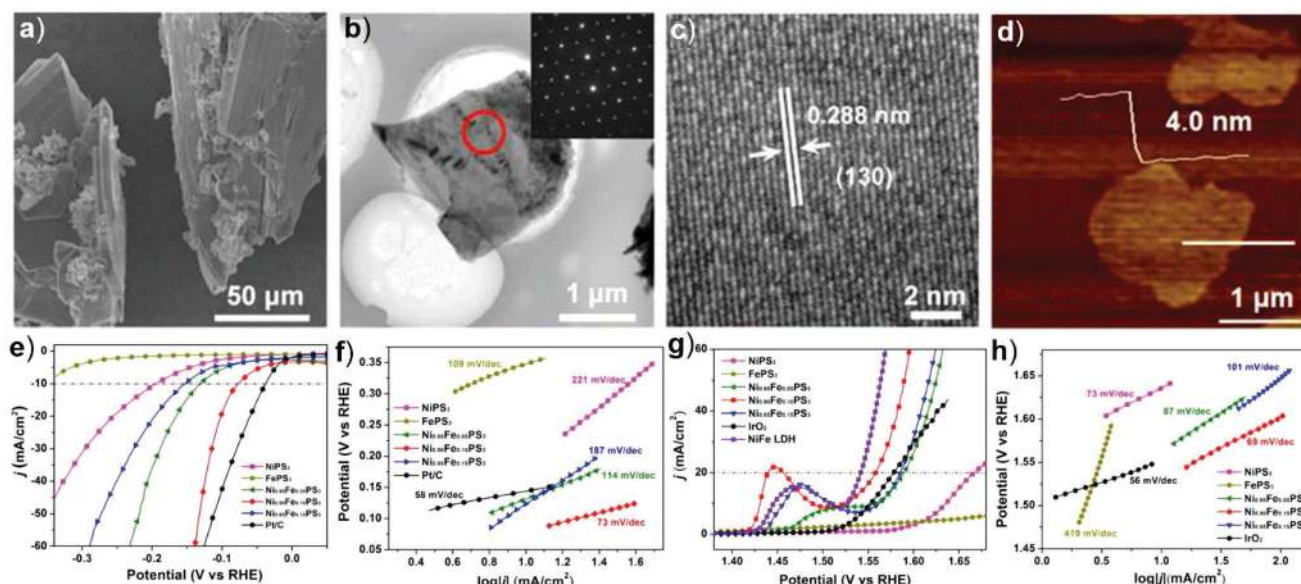
**ADVANCED
SCIENCE NEWS**

www.advancedsciencenews.com

**ADVANCED
FUNCTIONAL
MATERIALS**

www.afm-journal.de

Figure 18. a) SEM image of bulk $Ni_{0.9}Fe_{0.1}PS_3$ crystals. b) TEM image of $NiPS_3$ nanosheets. Inset: SAED in d). c) HRTEM image of $Ni_{0.9}Fe_{0.1}PS_3$ along the [001] zone axis. d) AFM images of the as-exfoliated $Ni_{0.9}Fe_{0.1}PS_3$ nanosheets. e) J–V curves after iR correction of $FePS_3$, $NiPS_3$, and various $Ni_{1-x}Fe_xPS_3$ electrocatalysts in comparison to 20 wt% Pt/C commercial catalyst. f) Tafel plots for the data presented in (e). g) J–V curves and h) Tafel plots after iR correction of OER performance of $FePS_3$, $NiPS_3$, and various $Ni_{1-x}Fe_xPS_3$ samples in comparison to IrO_2 and NiFe LDH. Reproduced with permission.[100] Copyright 2017, American Chemical Society.

the $FePS_3$ and $NiPS_3$ nanosheets have much poorer electrocatalytic activities compared to the exfoliated $Ni_{1-x}Fe_xPS_3$ ($x = 0.05$, 0.1, 0.15) nanosheets that exhibited extremely high HER and OER activity and durability in the aqueous solution of 1 M KOH (Figure 18e–h). This is attributable to the increase of intrinsic conductivity and electrochemical active surface area. Interestingly, the results show that the $Ni_{0.9}Fe_{0.1}PS_3$ nanosheets, whose surface would be transformed into hydroxides as the real active species, serve as the OER electrocatalysts in alkaline media.

3.2. Electrochemical Storage

Despite being a very promising future green energy source, hydrogen suffers from the lack of efficient and safe storage systems. Layered compounds, in general, are thought to advance the technology of hydrogen storage owing to their ability to be reversibly intercalated with the corresponding ions. Promising performances were reported using MPX_3 compounds such as $MnPS_3$,[109] $NiPS_3$,[24] and $FePS_3$.[104] Hydrogen is assumed to be adsorbed on the surface, in the micropores, and in the interlayer spacing. The hydrogen sorption capacity over $MnPS_3$ at different temperatures and pressures can be observed from the work by Ismail et al. in **Figure 19**a.[109] $MnPS_3$ is found to exhibit an adsorption capacity of 0.7 wt% within 100 min and the same duration is required to desorb it completely. The capacity reaches to 2.9 wt% at an elevated pressure of 30 bar in 30 min; however, in this case, a longer duration is required for desorption. The hydrogen adsorption/desorption cycles do not affect their crystal structure, but the overall performance is altered by the crystallinity of the material. The effect of crystallinity of the $FePS_3$ powders in hydrogen sorption at 193 °C is illustrated in Figure 19b.[104] A linear progression can be

observed up to 20 bar in the hydrogen sorption isotherm wherein the hydrogen sorption capacity for single crystalline and polycrystalline $FePS_3$ is recorded as 2.2 wt% and 1.7%, respectively (Figure 19b). A well-ordered single crystalline phase and wider interplanar space are usually associated with better performance for hydrogen sorption efficiency.[104] These findings emphasize the favorability of MPX_3 compounds for hydrogen storage and, hence, many other members can be explored following these promising performances.

MPX_3 compounds find substantial application in secondary Li/Na ion batteries due to their ability to create sufficient paths of lithium ion and exhibit high electronic conductivity with excellent ions mobility (Section 1.2.5). A particularly advantageous feature of this family in lithium batteries emanates from the broader van der Waals gap compared to TMDs, which make the unit cell parameter of the MPX_3 compounds remain unaffected after lithium intercalation.[29,110] Therefore, they provide enough capacity for ions while maintaining structure stable during the charge–discharge cycles. It has also been suggested that the very good Li/Na ion storage for battery application is following the electrochemical reaction involving nine lithium atoms per molecule of MPX_3 intercalation, as follows[22,87,111]

$$MPX_3 + 9Li^+ + 9e^- \rightarrow 3Li_2X + Li_3P + M \tag{1}$$

The formation of lithium (the same works for sodium) phosphides and sulfides endows a better conductivity compared to the lithium/sodium oxides that are commonly formed from the metal oxide materials.[23,86] Thus, this family is expected to demonstrate a better rate and cycling performance with high specific capacity. The sufficient electron conduction and paths for lithium ions were corroborated via employing $FePS_3$ materials for lithium ion battery application.[112] In this set up, a
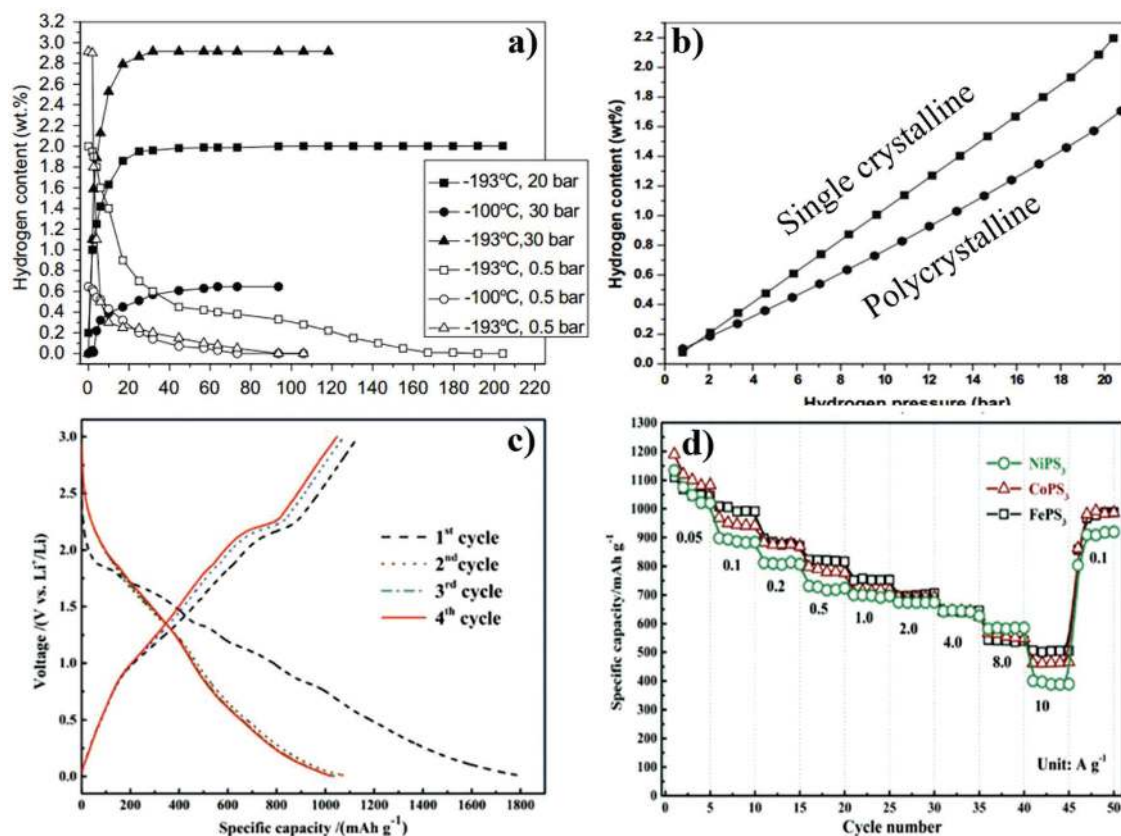
**ADVANCED
SCIENCE NEWS**
www.advancedsciencenews.com

**ADVANCED
FUNCTIONAL
MATERIALS**
www.afm-journal.de

Figure 19. a) Kinetics curves of $MnPS_3$ powders for H_2 sorption at different temperatures and pressures. Reproduced with permission.[109] Copyright 2010, Elsevier Ltd. b) Pressure-composition isotherms for single crystalline and polycrystalline $FePS_3$. Reproduced with permission.[104] Copyright 2010, Elsevier Ltd. c) Galvanostatic charge–discharge profiles of $NiPS_3$ nanosheet at 0.05 A g^{-1} and d) rate capabilities of MPS_3 (M = Fe, Co, Ni). Reproduced with permission.[23] Copyright 2017, Wiley-VCH.

reversible charge–discharge processes under 0.13 mA cm^{-2} at room temperature was demonstrated. Furthermore, the work by Yan and co-workers[23] is a typical experimental report demonstrating the Li/Na ions storage properties of $FePS_3$, $NiPS_3$, and $CoPS_3$ nanosheets. The clean surface, high crystallinity, high surface area, and better contact with the electrolyte or current collector endow superior performance. They exhibit significantly better performance of Li-ion/Na-ion storage compared to their bulk (<300 mA h g^{-1})[111,112] or sulfide counterparts (<1000 mA h g^{-1}).[113] The ultrathin nanosheets shorten the diffusion paths and accelerate the charge transfer process leading to a discharge and charge capacity of 1796 and 1100 mA h g^{-1} at a current density of 0.05 A g^{-1}, respectively (Figure 19c), with an initial Coulombic efficiency (CE) of 61.2%. The CE reaches almost 100% after the third cycle due to the minimized loss of capacity from side reactions, such as electrolyte decomposition and solid-electrolyte interphase formation. Collectively, the fourth cycle specific capacities at current densities of 0.05 and 10 A g^{-1} can be gleaned from Figure 19d as 1026 and 383 mA h g^{-1} ($NiPS_3$), 1046 and 506 mA h g^{-1} ($FePS_3$), and 1086 and 465 mA h g^{-1} ($CoPS_3$), respectively.

On top of their intrinsic property, the improvement with respect to Li/Na storage performance is more pronounced by employing different strategies such as polymer intercalation, hybrid structure formation, etc. The effect of polymer

intercalation in these materials has been investigated through intercalation with propylamine. In this case, the interlayer distance becomes further enlarged to allow easier ion accessibility and faster ion diffusion.[23] Hybrid structure formation also plays its own role in enhancing the performance as exhibited in Li_2S–$FePS_3$ composites where it appears to endow structural reversibility against the Li extraction/insertion reactions.[114] Moreover, elemental doping along with the formation of 0D and 2D nanohybrids has recently been reported[115] to elucidate the collective role of bimetallic MPX_3 ($Co_{0.5}Ni_{0.5}PS_3$) and graphene in Li ion storage. The electrochemical performance is associated with the insertion of Li ions into the layered space of the ($Co_{0.5}Ni_{0.5}PS_3$) lattice, which is accompanied by gradual reduction of Co^{2+} and Ni^{2+} to elemental Co and Ni; and the formation of Li_2S. The graphene support offers a conductive scaffold which contributes to the improved stability and rate performance.

3.3. Other Applications

The continual effort to explore the fascinating properties of metal phosphorus trichalcogenides also applies to many other applications. These materials are acknowledged for their high carrier mobility.[21] The recent experimental work by Lee et al.[116] demonstrates the thickness dependent tunneling transport properties
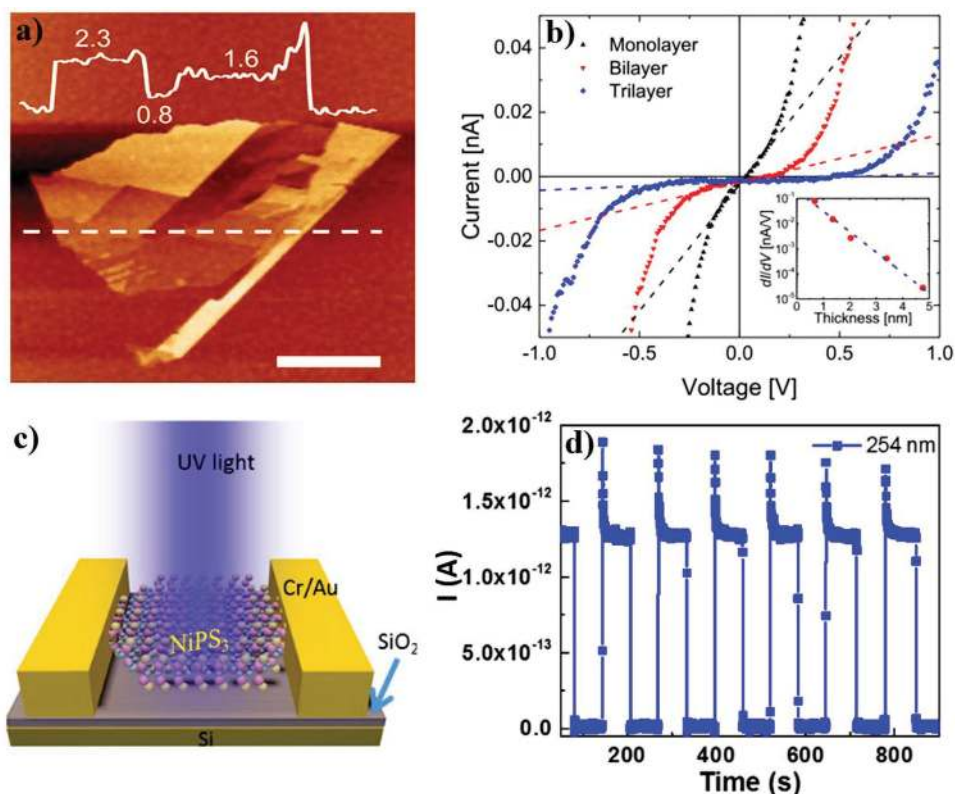
**ADVANCED
SCIENCE NEWS**
www.advancedsciencenews.com

**ADVANCED
FUNCTIONAL
MATERIALS**
www.afm-journal.de

Figure 20. a) AFM images depicting various thicknesses (monolayer to 6 layers) of MnPS$_3$ obtained via scotch-tape exfoliation of the CVT product (scale bar = 5 μm). b) I–V data at a low voltage region of monolayer, bilayer, and trilayer MnPS$_3$. The inset indicates that the slope of the linear behavior at low voltage decreases exponentially as the number of layers increases. Reproduced with permission.[116] Copyright 2016, AIP. c) A schematic and d) time-dependent photoresponse representing the applicability of ultrathin NiPS$_3$ as a promising UV photodetector. Reproduced with permission.[61] Copyright 2017, Wiley-VCH.

of MnPS$_3$. Flakes of various thicknesses, including mono layer and tens of layers (AFM image, **Figure 20**a), were obtained via the CVT method followed by scotch-tape exfoliation. A Schottky junction tunneling behavior was observed across the indium tin oxides (ITO)/MnPS$_3$/Pt-Ir junction with a dielectric breakdown strength of 5.41 mV cm^{-1}. Figure 20b shows that the conductance depends on the number of layers, which exponentially decreases with the increase of the thickness (i.e., the number of layers), as illustrated in the inset of Figure 20b. Moreover, the availability of ample elemental choices in the MPX$_3$ family enables the adjustment of bandgaps in the range of 1.3–3.5 eV (from near infrared to the UV region). This wide range spectrum suggests their optoelectronic application in a broad wavelength horizon. Recently, high photodetectivity of 1.22×10^{12} Jones and ultrafast rise times shorter than 5 ms have been observed[61] from ultrathin NiPS$_3$ (Figure 20c,d). The ease of integration with the Si substrate and the better performance comparable with a commercial GaN UV detector can initiate the investigation of many others in this family. It is, therefore, compelling to mention that the members in the family of MPX$_3$ can find many outstanding applications in various fields due to their unique properties compared to other 2D materials. For instance, the cleavage energy required for thinning their bulk to the atomic thickness level is smaller compared to that of graphite. This makes the fabrication of monolayer heterostructures by van der Waals stacking easier, paving the way to the realization

of unusual ferroelectric and magnetic properties.[20,95] Thus, it is interesting to note that the variation in metal components or in chalcogen components provides a conducive platform for the study of the incoming differences in spin-electron, electronic, or optoelectronic devices.

4. Future Perspectives

Layered MPX$_3$ compounds constitute members that spread over a wide range of the periodic table. The M^{II}, M^{I}, and M^{III} states are stably located in octahedral sulfur or selenium environments, which is a notable difference compared to TMDs, whose cationic components are in the form of the M^{IV} state. The strong ionic bond between M cations and [P$_2$X$_6$]$^{4-}$ endows MPX$_3$ materials with rich functionalities. These configuration features give rise to the unique chemical and physical properties as well as the key distinction from TMDs. Alteration in the size of metal atoms (M^{II}), electronegativity, and electronic configuration can be used to study the structural, catalytic, and magnetic variation of the phases. As to the substituted phases of M^{I}M^{III}PX$_3$, they present different cationic ordering from the original which is more pronounced in magnetism and ferroelectricity due to the cationic radius size ratio.

In this review, we have discussed the relation between crystal structure and component variations, unique properties,

**ADVANCED
SCIENCE NEWS**

www.advancedsciencenews.com

**ADVANCED
FUNCTIONAL
MATERIALS**

www.afm-journal.de

and progress in growth, characterization, and applications of MPX_3 crystals. The current growth status reveals the successful realization of ultrathin $NiPS_3$ and $MnPX_3$ nanosheets via the chemical vapor deposition method. It is reasonable to say that the growth of the MPX_3 monolayer, similar to the TMD monolayer, has yet to be thoroughly explored and prepared. More efforts should be devoted to the controllable growth of MPX_3. As mentioned, ionic bonding also contributes to the comparatively large bandgap range from 1.3 to 3.5 eV, which is unavailable for other 2D materials, indicating their potential application in optoelectronics and photo(electro)chemical catalysis. Another fascinating future direction would be designing heterostructures using MPX_3 as a component part and exploring the promising applications therein. At the same time, we envision that the magnetic 2D MPX_3 nanosheets play an indispensable role in spintronic devices. Their magnetism, especially the monolayer's, needs to be comprehensively studied via experimental methods in the 2D limit. Meanwhile, this rich magnetism and spin ordering in the electronic structure can find a promising future in catalysis. With the application of external magnetic field, the carrier mobility may be accelerated thereby boosting the catalytic properties. The high ions mobility and electronic transfer process are crucial for lithium and sodium batteries. Considering the general preparation approach, tunable interlayer spacing, and the ultrathin feature, such 2D MPX_3 crystals have great potential in energy conversion.

Conflict of Interest

The authors declare no conflict of interest.

[1] a) K. S. Novoselov, V. I. Falko, L. Colombo, P. R. Gellert, M. G. Schwab, K. Kim, *Nature* **2012**, *490*, 192; b) Q. Bao, K. P. Loh, *ACS Nano* **2012**, *6*, 3677; c) Y. Kim, S. S. Cruz, K. Lee, B. O. Alawode, C. Choi, Y. Song, J. M. Johnson, C. Heidelberger, W. Kong, S. Choi, K. Qiao, I. Almansouri, E. A. Fitzgerald, J. Kong, A. M. Kolpak, J. Hwang, J. Kim, *Nature* **2017**, *544*, 340; d) A. S. de Wijn, *Nature* **2016**, *539*, 502.

[2] D. Ovchinnikov, F. Gargiulo, A. Allain, D. J. Pasquier, D. Dumcenco, C. H. Ho, O. V. Yazyev, A. Kis, *Nat. Commun.* **2016**, *7*, 12391.

[3] a) V. Nicolosi, M. Chhowalla, M. G. Kanatzidis, M. S. Strano, J. N. Coleman, *Science* **2013**, *340*, 1226419; b) S.-Y. Xu, I. Belopolski, N. Alidoust, M. Neupane, G. Bian, C. Zhang, R. Sankar, G. Chang, Z. Yuan, C. C. Lee, S. M. Huang, H. Zheng, J. Ma, D. S. Sanchez, B. Wang, A. Bansil, F. Chou, P. P. Shibayev, H. Lin, S. Jia, M. Z. Hasan, *Science* **2015**, *349*, 613; c) Z. Ye, T. Cao, K. O. Brien, H. Zhu, X. Yin, Y. Wang, S. G. Louie, X. Zhang, *Nature* **2014**, *513*, 214; d) W. Xu, W. Liu, J. F. Schmidt, W. Zhao, X. Lu, T. Raab, C. Diederichs, W. Gao, D. V. Seletskiy, Q. Xiong, *Nature* **2016**, *541*, 62.

[4] a) F. Xia, H. Wang, Y. Jia, *Nat. Commun.* **2014**, *5*, 4458; b) H. Yuan, X. Liu, F. Afshinmanesh, W. Li, G. Xu, J. Sun, B. Lian, A. G. Curto, G. Ye, Y. Hikita, Z. Shen, S. C. Zhang, X. Chen, M. Brongersma, H. Y. Hwang, Y. Cui, *Nat. Nanotechnol.* **2015**, *10*, 707.

[5] a) C. T. Wee, L. Huang, J. N. Rui, L. Wang, N. H. Dihan Md, J. D. Thorin, S. K. Karuppannan, A. N. Christian, C. Lee, K. W. Ang, *Adv. Mater.* **2017**, *30*, 1705039; b) M. Buscema, D. J. Groenendijk, S. I. Blanter, G. A. Steele, H. S. J. van der Zant, A. Castellanos-Gomez, *Nano Lett.* **2014**, *14*, 3347; c) R. Fei, L. Yang, *Nano Lett.* **2014**, *14*, 2884.

[6] a) K. Watanabe, T. Taniguchi, H. Kanda, *Nat. Mater.* **2004**, *3*, 404; b) G. Cassabois, P. Valvin, B. Gil, *Nat. Photonics* **2016**, *10*, 262; c) Y. Kubota, K. Watanabe, O. Tsuda, T. Taniguchi, *Science* **2007**, *317*, 932; d) M. Schnell, A. García-Etxarri, A. J. Huber, K. Crozier, J. Aizpurua, R. Hillenbrand, *Nat. Photonics* **2009**, *3*, 287; e) M. Yankowitz, J. Xue, D. Cormode, J. D. Sanchez-Yamagishi, K. Watanabe, T. Taniguchi, P. Jarillo-Herrero, P. Jacquod, B. J. LeRoy, *Nat. Phys.* **2012**, *8*, 382; f) W. Yang, G. Chen, Z. Shi, C. C. Liu, L. Zhang, G. Xie, M. Cheng, D. Wang, R. Yang, D. Shi, K. Watanabe, T. Taniguchi, Y. Yao, Y. Zhang, G. Zhang, *Nat. Mater.* **2013**, *12*, 792; g) Z. Liu, L. Ma, G. Shi, W. Zhou, Y. Gong, S. Lei, X. Yang, J. Zhang, J. Yu, K. P. Hackenberg, A. Babakhani, J. C. Idrobo, R. Vajtai, J. Lou, P. M. Ajayan, *Nat. Nanotechnol.* **2013**, *8*, 119; h) S. Dai, Z. Fei, Q. Ma, A. S. Rodin, M. Wagner, A. S. McLeod, M. K. Liu, W. Gannett, W. Regan, K. Watanabe, T. Taniguchi, M. Thiemens, G. Dominguez, A. H. C. Neto, A. Zettl, F. Keilmann, P. Jarillo-Herrero, M. M. Fogler, D. N. Basov, *Science* **2014**, *343*, 1125.

[7] a) K. S. Novoselov, A. Mishchenko, A. Carvalho, A. H. Castro Neto, *Science* **2016**, *353*, 461; b) G. Fiori, F. Bonaccorso, G. Iannaccone, T. Palacios, D. Neumaier, A. Seabaugh, S. K. Banerjee, L. Colombo, *Nat. Nanotechnol.* **2014**, *9*, 768; c) L. Zhang, P. Bampoulis, A. N. Rudenko, Q. Yao, A. van Houselt, B. Poelsema, M. I. Katsnelson, H. J. W. Zandvliet, *Phys. Rev. Lett.* **2016**, *116*, 256804; d) A. A. Tonkikh, E. N. Voloshina, P. Werner, H. Blumtritt, B. Senkovskiy, G. Güntherodt, S. S. P. Parkin, Y. S. Dedkov, *Sci. Rep.* **2016**, *6*, 23547; e) Y. Liu, N. O. Weiss, X. Duan, H. C. Cheng, Y. Huang, X. Duan, *Nat. Rev. Mater.* **2016**, *1*, 16042.

[8] a) P. Goli, J. Khan, D. Wickramaratne, R. K. Lake, A. A. Balandin, *Nano Lett.* **2012**, *12*, 5941; b) X. Xi, L. Zhao, Z. Wang, H. Berger, L. Forró, J. Shan, K. F. Mak, *Nat. Nanotechnol.* **2015**, *10*, 765.

[9] a) X. Wang, A. M. Jones, K. L. Seyler, V. Tran, Y. Jia, H. Zhao, H. Wang, L. Yang, X. Xu, F. Xia, *Nat. Nanotechnol.* **2015**, *10*, 517; b) M. A. McGuire, G. Clark, S. Kc, W. M. Chance, G. E. Jellison, V. R. Cooper, X. Xu, B. C. Sales, *Phys. Rev. Mater.* **2017**, *1*, 014001.

[10] H. Cai, B. Chen, G. Wang, E. Soignard, A. Khosravi, M. Manca, X. Marie, L. Y. Chang Shery, B. Urbaszek, S. Tongay, *Adv. Mater.* **2017**, *29*, 1605551.

**ADVANCED
SCIENCE NEWS**

www.advancedsciencenews.com

**ADVANCED
FUNCTIONAL
MATERIALS**

www.afm-journal.de

[11] M. Chhowalla, H. S. Shin, G. Eda, L. J. Li, K. P. Loh, H. Zhang, *Nat. Chem.* **2013**, *5*, 263.

[12] a) T. Roy, M. Tosun, X. Cao, H. Fang, D. H. Lien, P. Zhao, Y. Z. Chen, Y. L. Chueh, J. Guo, A. Javey, *ACS Nano* **2015**, *9*, 2071; b) S. Kawai, A. S. Foster, T. Björkman, S. Nowakowska, J. Björk, F. F. Canova, L. H. Gade, T. A. Jung, E. Meyer, *Nat. Commun.* **2016**, *7*, 11559; c) X. Wang, F. Xia, *Nat. Mater.* **2015**, *14*, 264.

[13] K. F. Mak, C. Lee, J. Hone, J. Shan, T. F. Heinz, *Phys. Rev. Lett.* **2010**, *105*, 136805.

[14] a) M. J. Allen, V. C. Tung, R. B. Kaner, *Chem. Rev.* **2010**, *110*, 132; b) Y. Liu, X. Hua, C. Xiao, T. Zhou, P. Huang, Z. Guo, B. Pan, Y. Xie, *J. Am. Chem. Soc.* **2016**, *138*, 5087; c) F. Wang, Y. Li, A. Shifa Tofik, K. Liu, F. Wang, Z. Wang, P. Xu, Q. Wang, J. He, *Angew. Chem., Int. Ed.* **2016**, *128*, 7033; d) L. Yang, H. Hong, Q. Fu, Y. Huang, J. Zhang, X. Cui, Z. Fan, K. Liu, B. Xiang, *ACS Nano* **2015**, *9*, 6478.

[15] Y. Li, Y.-L. Li, C. M. Araujo, W. Luo, R. Ahuja, *Catal. Sci. Technol.* **2013**, *3*, 2214.

[16] J. Kang, S. Tongay, J. Zhou, J. Li, J. Wu, *Appl. Phys. Lett.* **2013**, *102*, 012111.

[17] C. Friedel, *Compt. Rend.* **1894**, *119*, 260.

[18] G. Ouvrard, R. Brec, J. Rouxel, *Mater. Res. Bull.* **1985**, *20*, 1181.

[19] L. Ferrand, *Bull. Soc. Chie. Fr.* **1895**, *13*, 115.

[20] K. z. Du, X. z. Wang, Y. Liu, P. Hu, M. I. B. Utama, C. K. Gan, Q. Xiong, C. Kloc, *ACS Nano* **2016**, *10*, 1738.

[21] X. Zhang, X. Zhao, D. Wu, Y. Jing, Z. Zhou, *Adv. Sci.* **2016**, *3*, 1600062.

[22] Y. V. Kuzminskii, B. M. Voronin, N. N. Redin, *J. Power Sources* **1995**, *55*, 133.

[23] Q. Liang, Y. Zheng, C. Du, Y. Luo, J. Zhang, B. Li, Y. Zong, Q. Yan, *Small Methods* **2017**, *1*, 1700304.

[24] N. Ismail, M. Madian, A. A. El-Meligi, *J. Alloys Compd.* **2014**, *588*, 573.

[25] C. E. Byvik, B. Reichman, D. W. Coleman, *J. Electrochem. Soc.* **1982**, *129*, 237.

[26] G. Le Flem, R. Brec, G. Ouvard, A. Louisy, P. Segransan, *J. Phys. Chem. Solids* **1982**, *43*, 455.

[27] K. Kurosawa, S. Saito, Y. Yamaguchi, *J. Phys. Soc. Jpn.* **1983**, *52*, 3919.

[28] X. Li, X. Wu, J. Yang, *J. Am. Chem. Soc.* **2014**, *136*, 11065.

[29] R. Brec, *Solid State Ionics* **1986**, *22*, 3.

[30] A. Susner Michael, M. Chyasnavichyus, A. McGuire Michael, P. Ganesh, P. Maksymovych, *Adv. Mater.* **2017**, *29*, 1602852.

[31] G. Kliche, Z. *Naturforsch., A: Phys., Phys. Chem., Kosmophys.* **1983**, *38A*, 1133.

[32] J. Banys, J. Macutkevic, R. Grigalaitis, J. Vysochanskii, *Solid State Ionics* **2008**, *179*, 79.

[33] X. Yan, X. Chen, J. Qin, *Mater. Res. Bull.* **2011**, *46*, 235.

[34] a) Y. Vysochanskii, M. Medulych, A. Molnar, K. Glukhov, A. Dziaugys, J. Banys, R. Yevych, M. Maior, *Ferroelectrics* **2014**, *462*, 117; b) B. Zapeka, M. Kostyrko, I. Martynyuk-Lototska, R. Vlokh, *Philos. Mag.* **2015**, *95*, 382.

[35] J. U. Lee, S. Lee, J. H. Ryoo, S. Kang, T. Y. Kim, P. Kim, C. H. Park, J. G. Park, H. Cheong, *Nano Lett.* **2016**, *16*, 7433.

[36] F. Wang, T. A. Shifa, P. He, Z. Cheng, J. Chu, Y. Liu, Z. Wang, F. Wang, Y. Wen, L. Liang, J. He, *Nano Energy* **2017**, *40*, 673.

[37] M. Z. Jandali, G. Eulenberger, H. Hahn, *Z. Anorg. Allg. Chem.* **2004**, *447*, 105.

[38] F. Fournier, J. Berthelot, Y. L. Pascal, *Tetrahedron* **1984**, *40*, 339.

[39] A. Wiedenmann, J. Rossat-Mignod, A. Louisy, R. Brec, J. Rouxel, *Solid State Commun.* **1981**, *40*, 1067.

[40] S. Jörgens, A. Mewis, *Z. Anorg. Allg. Chem.* **2003**, *630*, 51.

[41] R. Brec, G. Ouvrard, A. Louisy, J. Rouxel, *Ann. Chim.* **1980**, *5*, 499.

[42] S. Lee, P. Colombet, G. Ouvrard, R. Brec, *Inorg. Chem.* **1988**, *27*, 1291.

[43] Z. Ouili, A. Leblanc, P. Colombet, *J. Solid State Chem.* **1987**, *66*, 86.

[44] V. Maisonneuve, V. B. Cajipe, A. Simon, R. Von Der Muhll, J. Ravez, *Phys. Rev. B* **1997**, *56*, 10860.

[45] V. Maisonneuve, M. Evain, C. Payen, V. B. Cajipe, P. Molinié, *J. Alloys Compd.* **1995**, *218*, 157.

[46] G. Burr, E. Durand, M. Evain, R. Brec, *J. Solid State Chem.* **1993**, *103*, 514.

[47] R. Shannon, *Acta Crystallogr., Sect. A* **1976**, *32*, 751.

[48] M. A. Gave, D. Bilc, S. D. Mahanti, J. D. Breshears, M. G. Kanatzidis, *Inorg. Chem.* **2005**, *44*, 5293.

[49] R. Brec, D. M. Schleich, G. Ouvrard, A. Louisy, J. Rouxel, *Inorg. Chem.* **1979**, *18*, 1814.

[50] Y. Ohno, K. Hirama, *J. Solid State Chem.* **1986**, *63*, 258.

[51] F. S. Khumalo, H. P. Hughes, *Phys. Rev. B* **1981**, *23*, 5375.

[52] H. Mercier, Y. Mathey, E. Canadell, *Inorg. Chem.* **1987**, *26*, 963.

[53] V. Zhukov, S. Alvarez, D. Novikov, *J. Phys. Chem. Solids* **1996**, *57*, 647.

[54] B. L. Chittari, Y. Park, D. Lee, M. Han, A. H. MacDonald, E. Hwang, J. Jung, *Phys. Rev. B* **2016**, *94*, 184428.

[55] N. Kurita, K. Nakao, *J. Phys. Soc. Jpn.* **1987**, *56*, 4455.

[56] Y. M. Vysochanskii, V. A. Stephanovich, A. A. Molnar, V. B. Cajipe, X. Bourdon, *Phys. Rev. B* **1998**, *58*, 9119.

[57] a) M. Piacentini, F. S. Khumalo, C. G. Olson, J. W. Anderegg, D. W. Lynch, *Chem. Phys.* **1982**, *65*, 289; b) E. J. K. B. Banda, *J. Phys. C: Solid State Phys.* **1986**, *19*, 7329.

[58] a) A. C. Ferrari, D. M. Basko, *Nat. Nanotechnol.* **2013**, *8*, 235; b) A. Gupta, G. Chen, P. Joshi, S. Tadigadapa, Eklund, *Nano Lett.* **2006**, *6*, 2667; c) A. C. Ferrari, J. C. Meyer, V. Scardaci, C. Casiraghi, M. Lazzeri, F. Mauri, S. Piscanec, D. Jiang, K. S. Novoselov, S. Roth, A. K. Geim, *Phys. Rev. Lett.* **2006**, *97*, 187401; d) H. Li, Q. Zhang, R. Yap Chin Chong, K. Tay Beng, T. Edwin Teo Hang, A. Olivier, D. Baillargeat, *Adv. Funct. Mater.* **2012**, *22*, 1385.

[59] W. Xingzhi, D. Kezhao, L. Yu Yang Fredrik, H. Peng, Z. Jun, Z. Qing, O. Man Hon Samuel, L. Xin, G. Chee Kwan, S. Pinaki, K. Christian, X. Qihua, *2D Mater.* **2016**, *3*, 031009.

[60] C.-T. Kuo, M. Neumann, K. Balamurugan, H. J. Park, S. Kang, H. W. Shiu, J. H. Kang, B. H. Hong, M. Han, T. W. Noh, J.-G. Park, *Sci. Rep.* **2016**, *6*, 20904.

[61] J. Chu, F. Wang, L. Yin, L. Lei, C. Yan, F. Wang, Y. Wen, Z. Wang, C. Jiang, L. Feng, J. Xiong, Y. Li, J. He, *Adv. Funct. Mater.* **2017**, *27*, 1701342.

[62] a) N. Mounet, M. Gibertini, P. Schwaller, D. Campi, A. Merkys, A. Marrazzo, T. Sohier, I. E. Castelli, A. Cepellotti, G. Pizzi, N. Marzari, *Nat. Nanotechnol.* **2018**, *13*, 246; b) N. Miao, B. Xu, L. Zhu, J. Zhou, Z. Sun, *J. Am. Chem. Soc.* **2018**, *140*, 2417; c) B. Huang, G. Clark, E. Navarro-Moratalla, D. R. Klein, R. Cheng, K. L. Seyler, D. Zhong, E. Schmidgall, M. A. McGuire, D. H. Cobden, W. Yao, D. Xiao, P. Jarillo-Herrero, X. Xu, *Nature* **2017**, *546*, 270; d) K. L. Seyler, D. Zhong, D. R. Klein, S. Gao, X. Zhang, B. Huang, E. Navarro-Moratalla, L. Yang, D. H. Cobden, M. A. McGuire, W. Yao, D. Xiao, P. Jarillo-Herrero, X. Xu, *Nat. Phys.* **2018**, *14*, 277; e) S. Jiang, J. Shan, K. F. Mak, *Nat. Mater.* **2018**, *17*, 406; f) G. Abellán, C. Martí-Gastaldo, A. Ribera, E. Coronado, *Acc. Chem. Res.* **2015**, *48*, 1601; g) M. B. Sanders, K. M. Baroudi, J. W. Krizan, O. A. Mukadam, R. J. Cava, *Phys. Status Solidi B* **2016**, *253*, 2056.

[63] C. Felser, H. Fecher Gerhard, B. Balke, *Angew. Chem., Int. Ed.* **2007**, *46*, 668.

[64] P. A. Joy, S. Vasudevan, *Phys. Rev. B* **1992**, *46*, 5425.

[65] a) S. O. Evans John, D. O'Hare, R. Clement, A. Leaustic, P. Thuéry, *Adv. Mater.* **2004**, *7*, 735; b) T. Wataru, M. Toshihiro, W. Tadataka, T. Kouichi, M. Kazuyuki, U. Yoshiya, T. Yoshiki, *J. Phys.: Conf. Ser.* **2009**, *150*, 042215; c) D. J. Goossens, *Eur. Phys. J. B* **2010**, *78*, 305; d) T. Masubuchi, X. Jin, K. Koyama, Y. Takahashi, K. Takase, Y. Uwatoko, Y. Takano, K. Sekizawa, *AIP Conf. Proc.* **2006**, *850*, 1279.

[66] C. C. Mayorga-Martinez, Z. Sofer, D. Sedmidubský, Š. Huber, A. Y. S. Eng, M. Pumera, *ACS Appl. Mater. Interfaces* **2017**, *9*, 12563.

[67] a) E. Ressouche, M. Loire, V. Simonet, R. Ballou, A. Stunault, A. Wildes, *Phys. Rev. B* **2010**, *82*, 100408; b) M. A. McGuire, H. Dixit, V. R. Cooper, B. C. Sales, *Chem. Mater.* **2015**, *27*, 612; c) A. R. Wildes, K. C. Rule, R. I. Bewley, M. Enderle, T. J. Hicks, *J. Phys.: Condens. Matter* **2012**, *24*, 416004; d) T. Asano, Y. Ajiro, M. Mekata, H. Yamazaki, N. Hosoito, T. Shinjo, H. Kikuchi, *Solid State Commun.* **1994**, *90*, 125; e) Y. Takano, N. Arai, A. Arai, Y. Takahashi, K. Takase, K. Sekizawa, *J. Magn. Magn. Mater.* **2004**, *272–276*, E593.

[68] D. J. Goossens, S. Brazier-Hollins, D. R. James, W. D. Hutchison, J. R. Hester, *J. Magn. Magn. Mater.* **2013**, *334*, 82.

[69] K. C. Rule, G. J. McIntyre, S. J. Kennedy, T. J. Hicks, *Phys. Rev. B* **2007**, *76*, 134402.

[70] A. R. Wildes, B. Roessli, B. Lebech, K. W. Godfrey, *J. Phys.: Condens. Matter* **1998**, *10*, 6417.

[71] N. Chandrasekharan, S. Vasudevan, *J. Phys.: Condens. Matter* **1994**, *6*, 4569.

[72] A. R. Wildes, V. Simonet, E. Ressouche, G. J. McIntyre, M. Avdeev, E. Suard, S. A. J. Kimber, D. Lançon, G. Pepe, B. Moubaraki, T. J. Hicks, *Phys. Rev. B* **2015**, *92*, 224408.

[73] a) L. J. Sandilands, J. X. Shen, G. M. Chugunov, S. Y. F. Zhao, S. Ono, Y. Ando, K. S. Burch, *Phys. Rev. B* **2010**, *82*, 064503; b) W. H. Ko, Z. X. Liu, T. K. Ng, P. A. Lee, *Phys. Rev. B* **2010**, *81*, 024414.

[74] N. Suzuki, H. Kamimura, *J Phys. Soc. Jpn.* **1973**, *35*, 985.

[75] D. J. Goossens, T. J. Hicks, *J. Phys.: Condens. Matter* **1998**, *10*, 7643.

[76] T. Masubuchi, H. Hoya, T. Watanabe, Y. Takahashi, S. Ban, N. Ohkubo, K. Takase, Y. Takano, *J. Alloys Compd.* **2008**, *460*, 668.

[77] J. Macutkevic, J. Banys, R. Grigalaitis, Y. Vysochanskii, *Phys. Rev. B* **2008**, *78*, 064101.

[78] X. Bourdon, A. R. Grimmer, V. B. Cajipe, *Phosphorus Res. Bull.* **1999**, *10*, 100.

[79] X. Bourdon, V. Maisonneuve, V. B. Cajipe, C. Payen, J. E. Fischer, *J. Alloys Compd.* **1999**, *283*, 122.

[80] A. Simon, J. Ravez, V. Maisonneuve, C. Payen, V. B. Cajipe, *Chem. Mater.* **1994**, *6*, 1575.

[81] E. Durand, G. Ouvrard, M. Evain, R. Brec, *Inorg. Chem.* **1990**, *29*, 4916.

[82] V. Shusta, I. Prits, P. Guranich, E. Gerzanich, A. Slivka, *Condens. Matter Phys.* **2007**, *49*, 91.

[83] A. Belianinov, Q. He, A. Dziaugys, P. Maksymovych, E. Eliseev, A. Borisevich, A. Morozovska, J. Banys, Y. Vysochanskii, S. V. Kalinin, *Nano Lett.* **2015**, *15*, 3808.

[84] M. A. Susner, A. Belianinov, A. Borisevich, Q. He, M. Chyasnavichyus, H. Demir, D. S. Sholl, P. Ganesh, D. L. Abernathy, M. A. McGuire, P. Maksymovych, *ACS Nano* **2015**, *9*, 12365.

[85] a) A. H. Thompson, M. S. Whittingham, *Mater. Res. Bull.* **1977**, *12*, 741; b) A. Le Méhauté, G. Ouvrard, R. Brec, J. Rouxel, *Mater. Res. Bull.* **1977**, *12*, 1191.

[86] X. Y. Yu, L. Yu, W. X. Lou, *Adv. Energy Mater.* **2015**, *6*, 1501333.

[87] P. J. S. Foot, T. Katz, S. N. Patel, B. A. Nevett, A. R. Pieecy, A. A. Balchin, *Phys. Status. Solidi A* **2006**, *100*, 11.

[88] L. Fabbrizzi, A. Poggi, *J. Chem. Soc., Chem. Commun.* **1980**, *0*, 646.

[89] W. Klingen, R. Ott, H. Hahn, *Z. Anorg. Allg. Chem.* **2004**, *396*, 271.

[90] A. U. Liyanage, M. M. Lerner, *RSC Adv.* **2012**, *2*, 474.

[91] K. S. Novoselov, A. K. Geim, S. V. Morozov, D. Jiang, Y. Zhang, S. V. Dubonos, I. V. Grigorieva, A. A. Firsov, *Science* **2004**, *306*, 666.

[92] a) J. Zheng, H. Zhang, S. Dong, Y. Liu, C. T. Nai, H. S. Shin, H. Y. Jeong, B. Liu, K. P. Loh, *Nat. Commun.* **2014**, *5*, 2995; b) H. Li, J. Wu, Z. Yin, H. Zhang, *Acc. Chem. Res.* **2014**, *47*, 1067; c) J. N. Coleman, *Acc. Chem. Res.* **2013**, *46*, 14; d) J. Zheng, H. Zhang, S. Dong, Y. Liu, C. Tai Nai, H. Suk Shin, H. Young Jeong, B. Liu, K. Ping Loh, *Nat. Commun.* **2014**, *5*, 2995; e) J. Lee, T. Y. Ko, J. H. Kim, H. Bark, B. Kang, S.-G. Jung, T. Park, Z. Lee, S. Ryu, C. Lee, *ACS Nano* **2017**, *11*, 10935; f) C. N. R. Rao, A. Nag, *Eur. J. Inorg. Chem.* **2010**, *2010*, 4244; g) K. S. Novoselov, D. Jiang, F. Schedin, T. J. Booth, V. V. Khotkevich, S. V. Morozov, A. K. Geim, *Proc. Natl. Acad. Sci. USA* **2005**, *102*, 10451.

[93] J. Liu, X. B. Li, D. Wang, W. M. Lau, P. Peng, L. M. Liu, *J. Chem. Phys.* **2014**, *140*, 054707.

[94] a) D. O. Dumcenco, H. Kobayashi, Z. Liu, Y. S. Huang, K. Suenaga, *Nat. Commun.* **2013**, *4*, 1351; b) D. J. Late, T. Doneux, M. Bougouma, *Appl. Phys. Lett.* **2014**, *105*, 233103; c) H. Li, Z. Yin, Q. He, H. Li, X. Huang, G. Lu, H. Fam Derrick Wen, Y. Tok Alfred Iing, Q. Zhang, H. Zhang, *Small* **2011**, *8*, 63; d) H. Li, G. Lu, Y. Wang, Z. Yin, C. Cong, Q. He, L. Wang, F. Ding, T. Yu, H. Zhang, *Small* **2013**, *9*, 1974; e) J. Late Dattatray, N. Shirodkar Sharmila, V. Waghmare Umesh, P. Dravid Vinayak, C. N. R. Rao, *ChemPhysChem* **2014**, *15*, 1592.

[95] Y. Guo, C. Liu, Q. Yin, C. Wei, S. Lin, T. B. Hoffman, Y. Zhao, J. H. Edgar, Q. Chen, S. P. Lau, J. Dai, H. Yao, H. S. P. Wong, Y. Chai, *ACS Nano* **2016**, *10*, 8980.

[96] a) V. Goyal, D. Teweldebrhan, A. A. Balandin, *Appl. Phys. Lett.* **2010**, *97*, 133117; b) J. Sotor, G. Sobon, W. Macherzynski, P. Paletko, K. Grodecki, K. M. Abramski, *Opt. Mater. Express* **2014**, *4*, 1; c) K. M. F. Shahil, M. Z. Hossain, V. Goyal, A. A. Balandin, *J. Appl. Phys.* **2012**, *111*, 054305.

[97] P. Ares, F. Aguilar-Galindo, D. Rodríguez-San-Miguel, A. Aldave Diego, S. Diaz-Tendero, M. Alcamf, F. Martín, J. Gómez-Herrero, F. Zamora, *Adv. Mater.* **2016**, *28*, 6332.

[98] C. R. Dean, A. F. Young, I. Meric, C. Lee, L. Wang, S. Sorgenfrei, K. Watanabe, T. Taniguchi, P. Kim, K. L. Shepard, J. Hone, *Nat. Nanotechnol.* **2010**, *5*, 722.

[99] D. Mukherjee, M. A. P., S. Sampath, *ACS Appl. Energy Mater.* **2018**, *1*, 220.

[100] B. Konkena, J. Masa, A. J. R. Botz, I. Sinev, W. Xia, J. Koßmann, R. Drautz, M. Muhler, W. Schuhmann, *ACS Catal.* **2017**, *7*, 229.

[101] R. F. Frindt, D. Yang, P. Westreich, *J. Mater. Res.* **2011**, *20*, 1107.

[102] D. Mukherjee, P. M. Austeria, S. Sampath, *ACS Energy Lett.* **2016**, *1*, 367.

[103] M. Binnewies, R. Glaum, M. Schmidt, P. Schmidt, *Z. Anorg. Allg. Chem.* **2013**, *639*, 219.

[104] N. Ismail, A. A. El-Meligi, Y. M. Temerk, M. Madian, *Int. J. Hydrogen Energy* **2010**, *35*, 7827.

[105] B. Song, K. Li, Y. Yin, T. Wu, L. Dang, M. Cabán-Acevedo, J. Han, T. Gao, X. Wang, Z. Zhang, J. R. Schmidt, P. Xu, S. Jin, *ACS Catal.* **2017**, *7*, 8549.

[106] A. Shifa Tofik, F. Wang, Z. Cheng, P. He, Y. Liu, C. Jiang, Z. Wang, J. He, *Adv. Funct. Mater.* **2018**, *28*, 1800548.

[107] a) M. Y. Lin, L. W. Hourng, C.-W. Kuo, *Int. J. Hydrogen Energy* **2012**, *37*, 1311; b) R. Gusmão, Z. Sofer, D. Sedmidubský, Š. Huber, M. Pumera, *ACS Catal.* **2017**, *7*, 8159.

[108] C. E. Byvik, B. T. Smith, B. Reichman, *Sol. Energy Mater.* **1982**, *7*, 213.

[109] N. Ismail, Y. M. Temerk, A. A. El-Meligi, M. A. Badr, M. Madian, *J. Solid State Chem.* **2010**, *183*, 984.

[110] J. Rouxel, R. Brec, *Annu. Rev. Mater. Sci.* **1986**, *16*, 137.

[111] Y. V. Kuz'minskii, B. M. Voronin, I. M. Petrushina, N. N. Redin, G. P. Prikhodko, *J. Power Sources* **1995**, *55*, 1.

[112] Y. Fujii, A. Miura, N. C. Rosero-Navarro, M. Higuchi, K. Tadanaga, *Electrochim. Acta* **2017**, *241*, 370.

[113] X. Rui, H. Tan, Q. Yan, *Nanoscale* **2014**, *6*, 9889.

[114] T. Takeuchi, H. Kageyama, K. Ogawa, K. Mitsuhara, K. Nakanishi, T. Ohta, A. Sakuda, H. Kobayashi, H. Sakaebe, Z. Ogumi, *Solid State Ionics* **2016**, *288*, 199.

[115] C. F. Du, Q. Liang, Q. Yan, *J. Nat. Gas Chem.* **2018**, *27*, 190.

[116] S. Lee, K. Y. Choi, S. Lee, B. H. Park, J. G. Park, *APL Mater.* **2016**, *4*, 086108.

[117] E. Prouzet, G. Ouvrard, R. Brec, *Mater. Res. Bull.* **1986**, *21*, 195.

[118] Z. Wang, R. D. Willett, R. A. Laitinen, D. A. Cleary, *Chem. Mater.* **1995**, *7*, 856.

[119] R. Pfeiff, R. Kniep, *J. Alloys Compd.* **1992**, *186*, 111.

[120] P. Colombet, A. Leblanc, M. Danot, J. Rouxel, *J. Solid State Chem.* **1982**, *41*, 174.

[121] A. Pfitzner, S. Seidlmayer, *Z. Anorg. Allg. Chem.* **2009**, *635*, 704.

[122] S. Lee, P. Colombet, G. Ouvrard, R. Brec, *Mater. Res. Bull.* **1986**, *21*, 917.

[123] G. Ouvrard, R. Brec, *Mater. Res. Bull.* **1988**, *23*, 1199.

[124] R. Pfeiff, R. Kniep, *Z. Naturforsch., B* **1993**, *48*, 1270.

[125] I. P. Studenyak, V. V. Mitrovcij, S. Kovacs Gy, M. I. Gurzan, O. A. Mykajlo, M. Vysochanskii Yu, V. B. Cajipe, *Phys. Status Solidi B* **2003**, *236*, 678.

[126] C. Calareso, V. Grasso, L. Silipigni, *J. Appl. Phys.* **1997**, *82*, 6228.

[127] H. Mutka, C. Payen, P. Molinié, J. L. Soubeyroux, P. Colombet, A. D. Taylor, *Phys. Rev. Lett.* **1991**, *67*, 497.

[128] C. Payen, H. Mutka, J. L. Soubeyroux, P. Molinié, P. Colombet, *J. Magn. Magn. Mater.* **1992**, *104–107*, 797.

[129] Y. Huang, E. Sutter, N. N. Shi, J. Zheng, T. Yang, D. Englund, H. J. Gao, P. Sutter, *ACS Nano* **2015**, *9*, 10612.